ON-ORBIT STRUCTURAL DYNAMIC PERFORMANCE OF A LARGE-DIAMETER ANTENNA

by

Deborah M. Wahls

Major paper submitted to the Faculty of the

Virginia Polytechnic Institute and State University

in partial fulfillment of the requirements for the degree of

MASTER OF SCIENCE

in

Systems Engineering

APPROVED:

L. Glenn Kraige

L. G. Kraige, Chairman

B. S. Blanchard

B. S. Blanchard

C. F. Reinholtz

C. F. Reinholtz

June, 1991
Blacksburg, Virginia

ON-ORBIT STRUCTURAL DYNAMIC PERFORMANCE OF A LARGE-DIAMETER ANTENNA

by

Deborah M. Wahls
Systems Engineering

Committee Chairman: Professor L. G. Kraige
Engineering Science and Mechanics

(ABSTRACT)

An analysis of the structural vibrational performance of a 15-meter-diameter antenna subject to representative onboard dynamic disturbances is presented. Antenna performance parameter limits are defined for the root-mean-square surface roughness, pointing error, and defocus. The antenna concept is described, and the generation of the finite-element model is explained. A subreflector scanning scenario which represents an onboard disturbance to the system is modeled with orthogonal excitation functions. A modal analysis performed on the antenna in both free-flying and platform-mounted configurations is discussed. The resulting mode shapes and natural frequencies are then input to a forced-response analysis, which is performed for each configuration with the onboard scanning disturbance. The impact of the resulting dynamic distortions on the antenna performance parameters (i.e., errors) is assessed. The distortions in the surface are determined to contribute to all three errors, the displacement of the subreflector adds to the pointing error and defocus, and the displacement of the vertex is a component of the defocus.

Based on the results of the analysis, the reflector support structure and feed mast of the low-frequency microwave radiometer as designed are capable of maintaining their

shapes within specifications for the assumed on-orbit disturbance. This is particularly true for the platform-mounted configuration which exhibits errors within their respective limits by at least an order of magnitude. This is also true for the free-flyer configuration surface roughness and defocus; however, the free-flyer configuration maximum pointing error is significantly closer to, yet still within, its specified limit.

Acknowledgments

I would like to extend my gratitude to Dr. L. Glenn Kraige for his advice and assistance in the preparation of this report. Thanks also to Dean Benjamin S. Blanchard and Dr. Charles F. Reinholtz for serving on my advisory committee and to Ms. Loretta Tickle for her assistance with all the paperwork and organization.

I would also like to express my appreciation to those who were members of the Spacecraft Analysis Branch and to those who are members of the Vehicle Analysis Branch at NASA Langley Research Center.

Finally, I would like to express my gratitude to my husband, Richard, for his love and understanding, and to my mother, Irene, for her support and encouragement.

And to Dad:

This is for you

I wish you could have seen it

Table of Contents

List of Figures

35. Pointing error about y-axis for platform-mounted antenna.
    (a) Error due to surface distortion.
    (b) Error due to subreflector displacement.
    (c) Combined error.
36. Total LFMR pointing error for platform-mounted antenna.
37. Defocus for platform-mounted antenna.
    (a) Defocus due to surface distortion.
    (b) Defocus due to subreflector displacement.
    (c) Defocus due to paraboloid vertex displacement.
38. Total LFMR defocus for platform-mounted antenna.

List of Tables

List of Symbols

D	diameter of primary reflector, m
{F}	force vector, N
F	subsatellite footprint diameter, km
f	focal length, m
f/D	ratio of focal length to diameter
f_l	frequency of line scans, Hz
f_n	natural vibration frequency, Hz
H	orbit altitude, km
I	mass moment of inertia, kg-m^2
I_{xx}, I_{yy}, I_{zz}	centroidal mass moments of inertia about local x, y, and z-axes, respectively, kg-m^2
I_{xy}, I_{yz}, I_{zx}	centroidal mass products of inertia with respect to local reference planes, kg-m^2
[k]	stiffness matrix, N/m
[m]	mass matrix, kg
M	moment, N-m
M_x	north-south input torque, N-m
$M_{x,\text{reset}}$	north-south input torque for reset maneuver, N-m
M_y	east-west input torque, N-m
t	time as measured from beginning of a line scan, s
t_l	time for east-west line scan, s
t_S	time for north-south step-down procedure, s
t_{TA}	time for turnaround procedure, s

[u]	transformation matrix between true and generalized displacements
{X}	modal vector
{x}	true displacement vector, m
$\{\ddot{x}\}$	acceleration vector, m/s^2
x,y,z	coordinate axes as defined in Figure 1
θ_x	north-south angular displacement, deg
$\theta_{x,\text{reset}}$	north-south angular displacement for reset maneuver, deg
λ	wavelength of operating frequency, m
$\Phi_{f,x}$	pointing error about x-axis due to feed/subreflector displacement, rad
$\Phi_{f,y}$	pointing error about y-axis due to feed/subreflector displacement, rad
$\Phi_{s,x}$	pointing error about x-axis due to surface distortion, rad
$\Phi_{s,y}$	pointing error about y-axis due to surface distortion, rad
Φ_t	total pointing error, rad
Φ_x	combined pointing error about x-axis, rad
Φ_y	combined pointing error about y-axis, rad
$\{\eta\}$	generalized displacement vector, 1/m
$\{\dot{\eta}\}$	generalized velocity vector, 1/(m-s)
$\{\ddot{\eta}\}$	generalized acceleration vector, 1/(m-s^2)
$\dot{\omega}$	angular acceleration, rad/s^2
ω_n	natural frequency (eigenvalue), rad/s
ω_x	north-south angular velocity, deg/s
$\dot{\omega}_x$	north-south angular acceleration, deg/s^2
$\omega_{x,max}$	maximum north-south angular velocity, deg/s
$\omega_{x,reset}$	north-south angular velocity for reset maneuver, deg/s
$\dot{\omega}_{x,reset}$	north-south angular acceleration for reset maneuver, deg/s^2

ω_y	east-west angular velocity, deg/s
$\dot{\omega}_y$	east-west angular acceleration, deg/s^2
$\omega_{y,av}$	average east-west scan rate (angular velocity) of subreflector, deg/s
$\omega_{y,beam}$	average east-west scan rate (angular velocity) of emitted beam, deg/s
ζ	structural damping ratio

Abbreviations and Acronyms:

DOF	degrees of freedom
FEM	finite-element model
GEO	geosynchronous Earth orbit
HFMS	high-frequency microwave sounder
LASS	Large Advanced Space Structures
LEO	low Earth orbit
LFMR	low-frequency microwave radiometer
PSR	Precision Segmented Reflector
rms	root mean square
SDRC	Structural Dynamics Research Corporation
TTSS	Tetrahedral Truss Structural Synthesizer

Chapter 1. Introduction

The purpose of this report is to assess the structural dynamic behavior of a large-diameter antenna which is a component of NASA's proposed Mission to Planet Earth [1]. There has recently been an increased concern for environmental issues and an increased interest in studying the Earth as a global system. The Mission to Planet Earth is a program to monitor and study the Earth's hydrologic, biogeochemical, and climate cycles on a global scale. The antenna concept described in this report will be instrumental in satisfying some of the science requirements of the mission so long as it is capable of retaining its geometric shape within specified limits. The goal of this report, therefore, is to examine the behavior of the antenna structure subject to a representative onboard disturbance and to determine whether the antenna can satisfy the science requirements.

The types of observations to be made in the Mission to Planet Earth include various surface, atmospheric, and oceanic changes that occur in the global Earth system because of both environmental and man-made conditions. These fluctuations must be quantified and analyzed in terms of their interaction with humanity. The resulting data will be instrumental in forecasting future global system events. NASA is proposing technology development programs to produce both the sensors to perform the necessary observations and the spacecraft and data handling technologies required to support these instruments.

The complement of spacecraft needed to support the desired observations will consist of low-inclination low Earth orbit (LEO), polar LEO, and geosynchronous Earth orbit (GEO) platforms, each carrying a payload of instruments and sensors. Each of the three types of platforms will provide an observation environment that is best suited for its specific instruments. The LEO platforms will provide low temporal resolution, high

spatial resolution, and global coverage, whereas the GEO platforms will provide improved temporal resolution and nearly hemispherical coverage but with reduced spatial resolution.

An assessment of the structural dynamic performance of a large antenna concept aboard a proposed geostationary platform is presented in this paper. The sequence of analyses employed may be applied to a wide range of on-orbit assessments of reflector antennas. A list of instruments and the proposed concept for the geostationary platform are provided in [2]. The platform configuration, illustrated in Figure 1, is a NASA Langley Research Center (LaRC) concept, derived from a configuration described in [3]. The coordinate system shown is fixed to the platform.

The geostationary platform concept supports 18 different scientific instruments with widely diverse requirements while providing a stiff, stable platform environment for pointing accuracy. Most of these instruments are relatively small compared with the platform, except for two large reflector antennas: the 7.5-m-diameter high-frequency microwave sounder (HFMS) and the 15-m-diameter low-frequency microwave radiometer (LFMR). These two antennas are a significant part of the structural configuration and could greatly impact the dynamic behavior of the platform. Each antenna was analyzed individually in terms of its structural behavior and its ability to perform within the operating constraints of the system. A discussion of the thermal structural behavior of the high-accuracy HFMS primary reflector is documented in [4].

The structural dynamic behavior of the 15-m-diameter LFMR subject to a representative on-orbit disturbance is addressed in the present paper. The large aperture and focal length of the LFMR make it the more flexible of the two antennas and therefore more susceptible to performance degradation caused by on-orbit dynamic disturbances. Computer-based finite element analysis was used to evaluate the vibrational characteristics and performance of the LFMR due to the many degrees of freedom of the antenna, which

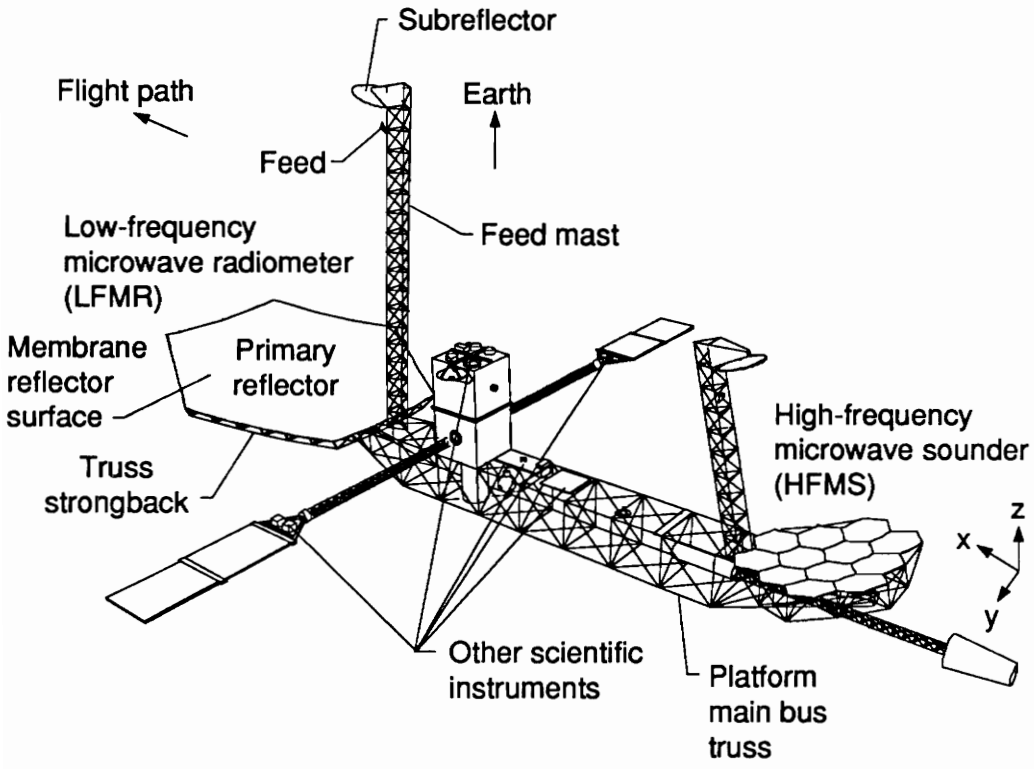

Figure 1. Geostationary Earth-science platform.

would require an excessive amount of computation if done by hand. An explanation of finite element analysis can be found in [5], where the fundamentals of vibration analysis are presented. The finite element method is also explained in [6]-[9] and matrix structural analysis, which is the basis for the finite element method, is described in [10]-[13].

There are numerous finite element tools available for the type of structural modeling and analysis presented in this report, including such industry-standards as NASTRAN [14] and PATRAN [15], as well as EAL [16] and I-DEAS [16], which are commonly used at NASA LaRC. Comparisons of various finite element analysis software packages are presented in [18]-[20]. For the present study, much of the modeling and all of the analysis was done using the I-DEAS software package, which is included in the software comparisons of both [18] and [19]. I-DEAS has been used previously for antenna structural analysis ([21] and [22]), and the results of [21] were cross-checked and confirmed with EAL results. I-DEAS is user-friendly, menu-driven, and graphics-oriented, and is often used as a pre- and post-processor in conjunction with an external structural analysis program such as NASTRAN (see, for example, [18] and [23]). One of the conclusions drawn in [18] is that the CPU time for an I-DEAS analysis run is substantially less than that for a comparable NASTRAN run. The use of the I-DEAS analysis capabilities (along with its pre- and post-processing capabilities) is suggested when possible. This also helps to avoid the transfer of data files between I-DEAS and an external analysis program since data transfer within I-DEAS is performed internally, thereby reducing overall analysis time.

The forthcoming chapters of this report are summarized below, along with descriptions of the specific tools and techniques used for each phase of the study. A study flowchart including the various tools used is illustrated in Figure 2.

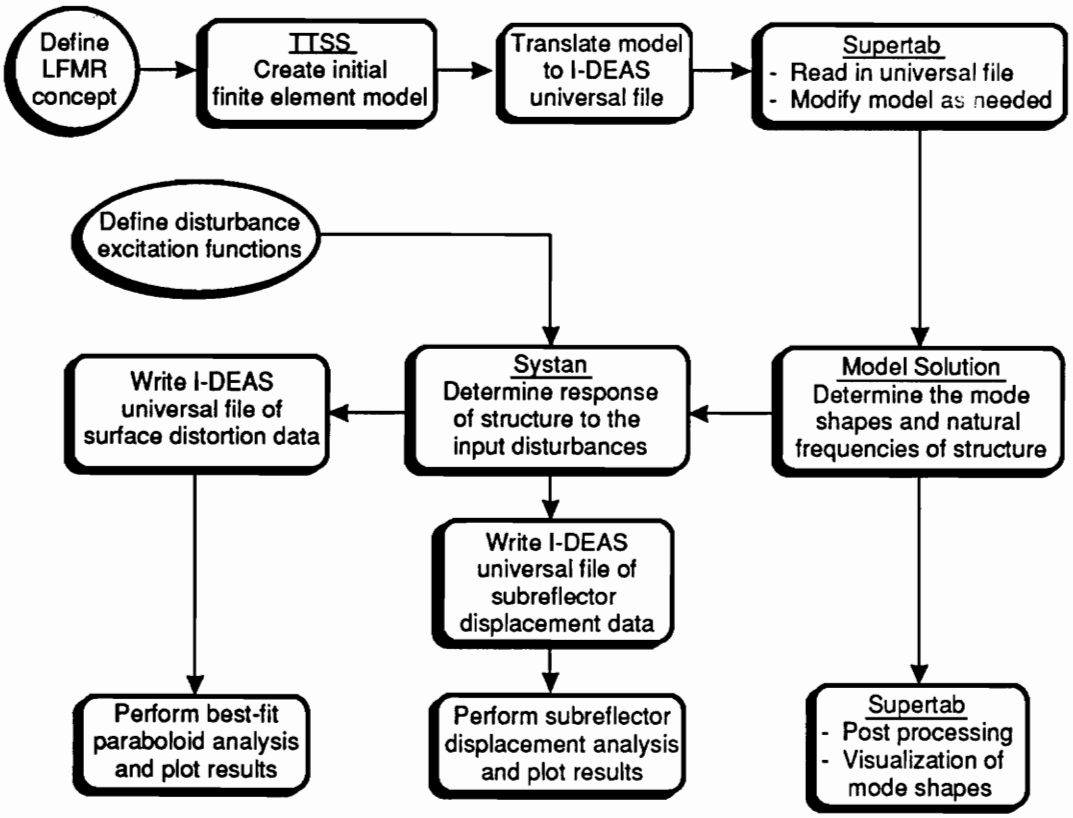

Figure 2. Study flowchart.

The antenna structure proposed for the LFMR in the present study, which is based upon existing technology and which should meet the mass and volume constraints of the transportation system [24], is discussed in Chapter 2. The antenna structural model is described. The Tetrahedral Truss Structure Synthesizer (TTSS, [25]) and Supertab [26] were used for generating the finite element model of the LFMR. TTSS, which is part of the Large Advanced Space Structures (LASS) program [25], was used to generate the antenna truss support structure. Based on user-input information such as antenna diameter, number of bays, focal length-to-diameter ratio (*f/D*), structural-element physical and material properties, and hinge and joint specifications, TTSS estimates structural element sizes and masses and generates a finite element model for use by a structural analysis program. For the present application, the TTSS model was transferred to Supertab, which is a part of the I-DEAS software package. This transfer was done by converting the TTSS output file to the I-DEAS universal file format and then reading this universal file into Supertab. Supertab is an interactive, menu-driven program used to construct, modify, and visualize finite-element models prior to structural analysis, and to graphically display the results of such an analysis. In Supertab other antenna components (including feed, subreflector, and feed mast) were modeled and added to the TTSS-generated truss model.

The results of a modal analysis performed on the LFMR finite element model are presented in Chapter 3. Two configurations were examined, and these are described along with their resulting mode shapes and natural frequencies of vibration. The modal analysis was performed using I-DEAS Model Solution [27], which determines the mode shapes and natural frequencies by calculating the eigenvalues and eigenvectors of the undamped, unforced vibration equation

$$[m]\{\ddot{x}\} + [k]\{x\} = \{0\}$$

where [m] is the mass matrix, [k] is the stiffness matrix, {x} is the displacement vector, $\{\ddot{x}\}$ is the acceleration vector, and the corresponding eigenvalue/eigenvector equation is

$$[k]\{X\} - \omega_n^2[m]\{X\} = \{0\}$$

where {X} and ω_n are the eigenvectors (mode shapes) and eigenvalues (natural frequencies), respectively. Once the mode shapes and natural frequencies were determined, Supertab was used for post-processing and graphic display of the mode shapes.

The formulation of the excitation functions used to simulate representative on-orbit disturbances is explained in Chapter 4. A subreflector scanning scenario is modeled with orthogonal excitation functions with harmonic torque impulses.

The forced response analysis of the LFMR is presented in Chapter 5, where geometric performance criteria are established and the analysis procedure is reviewed. The performance criteria consist of maximum allowable surface roughness, pointing error, and defocus. The forced response analysis was performed using I-DEAS Systan [28], which incorporates the mode shapes from Model Solution (Chapter 3) and the excitation functions formulated in Chapter 4 to solve

$$\{\ddot{\eta}\} + 2\zeta\omega_n\{\dot{\eta}\} + \omega_n^2\{\eta\} = [u]^T\{F\}$$

where {F} is the vector of applied forces (i.e. excitation functions), ζ represents the internal structural damping, and

$$\{x\} = [u]\{\eta\}$$

where $\{x\}$ and $\{\eta\}$ represent the true and generalized nodal displacements, respectively, and [u] is the the transformation matrix between them. The true nodal displacements represent the physical displacement of the truss nodes from their optimum (undistorted) locations. Nodal displacement data were calculated at a representative set of reflector surface nodes as well as the subreflector node. A program called Antperf, based on a surface accuracy routine described in [25] and [29], was then used to perform a best-fit paraboloid analysis, comparing the distorted surface nodes with their undistorted locations in order to calculate the resulting root-mean-squared (rms) surface roughness, pointing error, and defocus of the LFMR. Antperf uses Supertab finite element data to determine the shape of the undistorted paraboloid and Systan dynamic displacement data to calculate the best-fit paraboloid through the distorted nodes at each time step. The program then compares these data at each time step to determine the change in surface roughness, pointing direction, focal length, and x,y,z coordinates of the best-fit paraboloid vertex as compared with the undistorted shape. The Antperf output data and the Systan subreflector displacement data were then transferred back into Supertab for post-processing, combination (as appropriate), graphic display, and Fast Fourier Transform analysis of the dynamic response curves to determine specific modal contributions to each type of error.

The results are explained in Chapter 6, which includes plots of the time variations of each of the antenna errors (for both configurations) and the various components of these errors, as appropriate. Each plot is explained in terms of its maximum magnitude as well as its dynamic behavior (i.e., modal contributions). Concluding remarks are presented in Chapter 7.

Chapter 2. LFMR Design and Structural Model

The LFMR must operate (i.e., receive data) at frequencies of 6, 10, 18, 21, and 37 GHz [30] to meet the science requirements for the various measurements it will make. (Although the LFMR is a receiver antenna, this paper will refer occasionally to its "emitted beam." It should be noted that this is done for clarity in the explanation of various aspects of the performance of the antenna, which is the same for an emitter as for a receiver.) The antenna will monitor precipitation at frequencies of 18, 21, and 37 GHz, and observations of snow will be conducted at 18 and 37 GHz. The ocean will be observed at frequencies of 6, 10, and 18 GHz to measure surface temperature, surface wind, wind vector curl, surface geostrophic currents, and the motion of high wind patterns. Sea ice will be monitored at 10, 18, and 37 GHz.

The 15-m-diameter LFMR configuration used in this study is illustrated in Figure 3. Its reflector is offset fed so as to avoid blockage of the signal by the feed system. Cassegrain geometry, i.e., folded optics, is used so that scanning may be performed by rotating a subreflector rather than the feed system and its associated waveguides. A high effective ratio of focal length to diameter (f/D) of 1.5 is needed to retain accuracy during scanning maneuvers. The geometry of the LFMR, illustrated in Figure 4, is dictated by these factors as well as the geometry of the geostationary platform [2]. The relative sizes of the various LFMR components were selected consistent with an effort to minimize overall antenna mass and to avoid blocking the view of either the other instruments or the LFMR itself. All this yields a system consisting of a paraboloidal primary reflector with an extended feed mast that supports a subreflector and an electronic feed system. A mass summary of these components is shown in Table 1, and the finite-element model (FEM) is

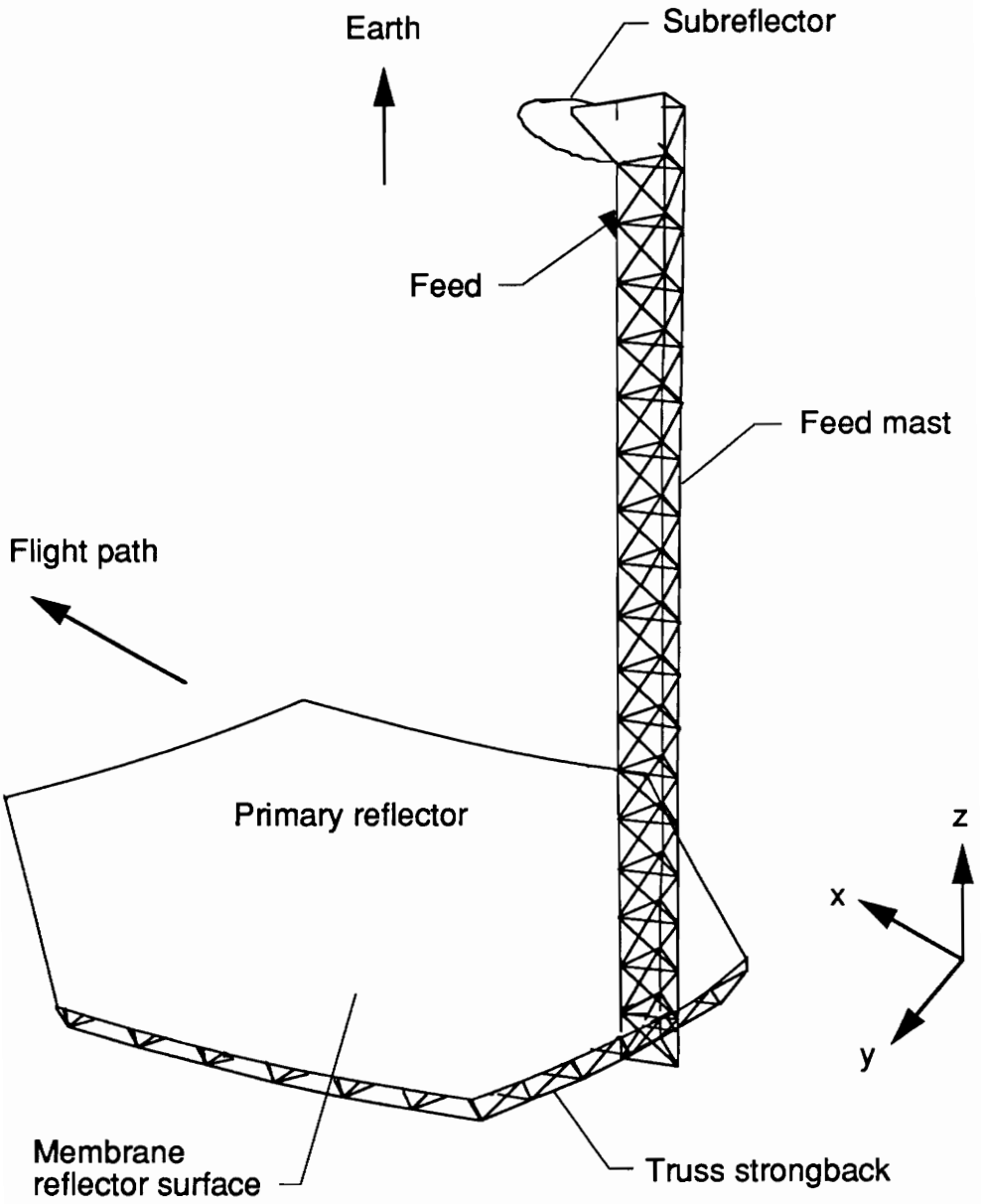

Figure 3. Low-frequency microwave radiometer (LFMR).

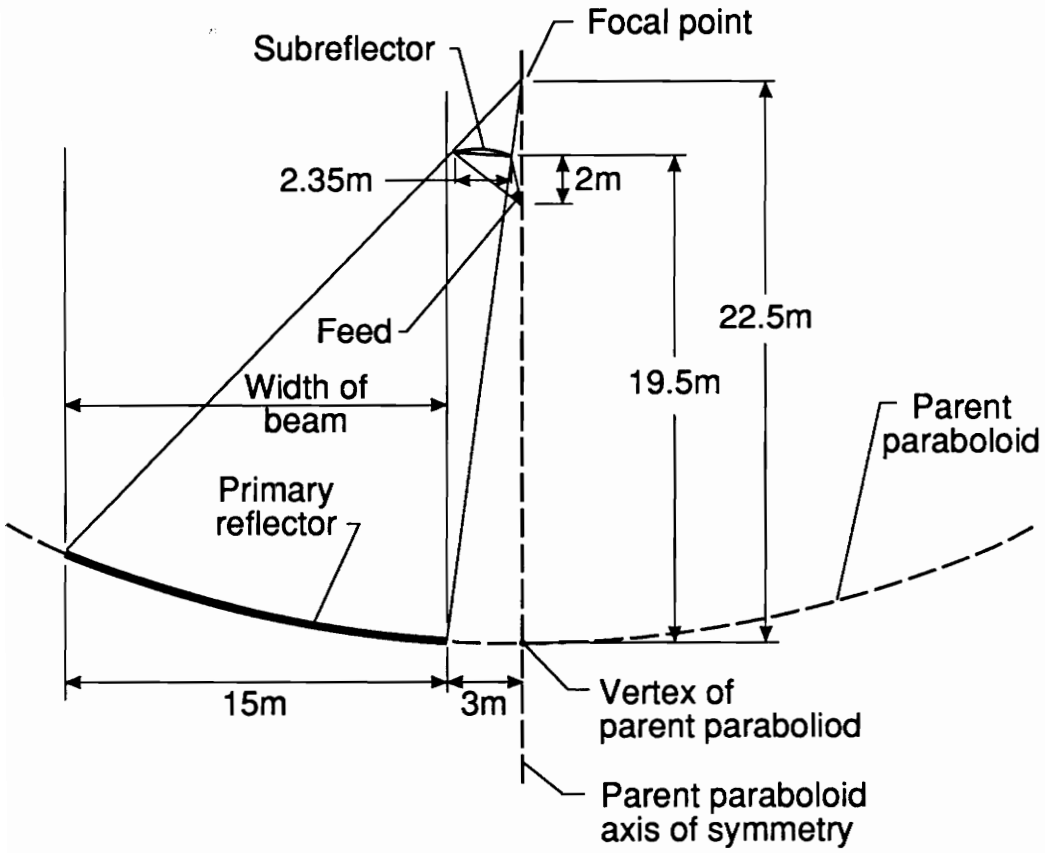

Figure 4. LFMR Cassegrain geometry.

Table 1. Low-frequency microwave radiometer (LFMR) mass summary.

Component	Mass, kg
Strongback	250
Reflector surface	3
Mast	95
Feed	443
Subreflector	52
Total	**843**

shown in Figure 5. A description of the main structural components of the LFMR follows.

Primary Reflector

The primary reflector is a 15-m-diameter, offset-fed paraboloid with its edge offset from the vertex of the parent paraboloid by 3 m, as shown in Figure 4. It consists of a tetrahedral truss structure (referred to here as a "strongback") supporting a membrane reflector surface. The membrane, made of 0.5-mil-thick aluminized Du Pont Kapton (1.42 g/cm^3), is attached to the strongback at each of the strongback top-surface joints. An assumption is made that no "pillowing" of the membrane surface exists between the connection points, which implies the use of additional tie cords between the strongback joints and the membrane. The purpose of the strongback is to provide a stiff, stable support for the membrane surface to minimize the distortion of the overall reflector shape.

The truss configuration selected for this study is that of the General Dynamics GEOTRUSS [31], which is a 12-bay tetrahedral truss composed of graphite/epoxy composite tube members with aluminum alloy joints and end fittings. It was selected for this configuration because of its advanced level of development and its lightweight, high-strength characteristics. The physical and material properties of the truss tube elements are listed in Table 2.

The primary reflector portion of the FEM shown in Figure 5 consists of 235 nodes, 954 beam elements, and 362 lumped mass elements (not shown). Each node represents the location of a strongback joint and supports a lumped mass element representing the mass of the appropriate joint and end fittings. Each node on the reflector side (top surface) of the strongback supports an additional lumped mass element representing the appropriate

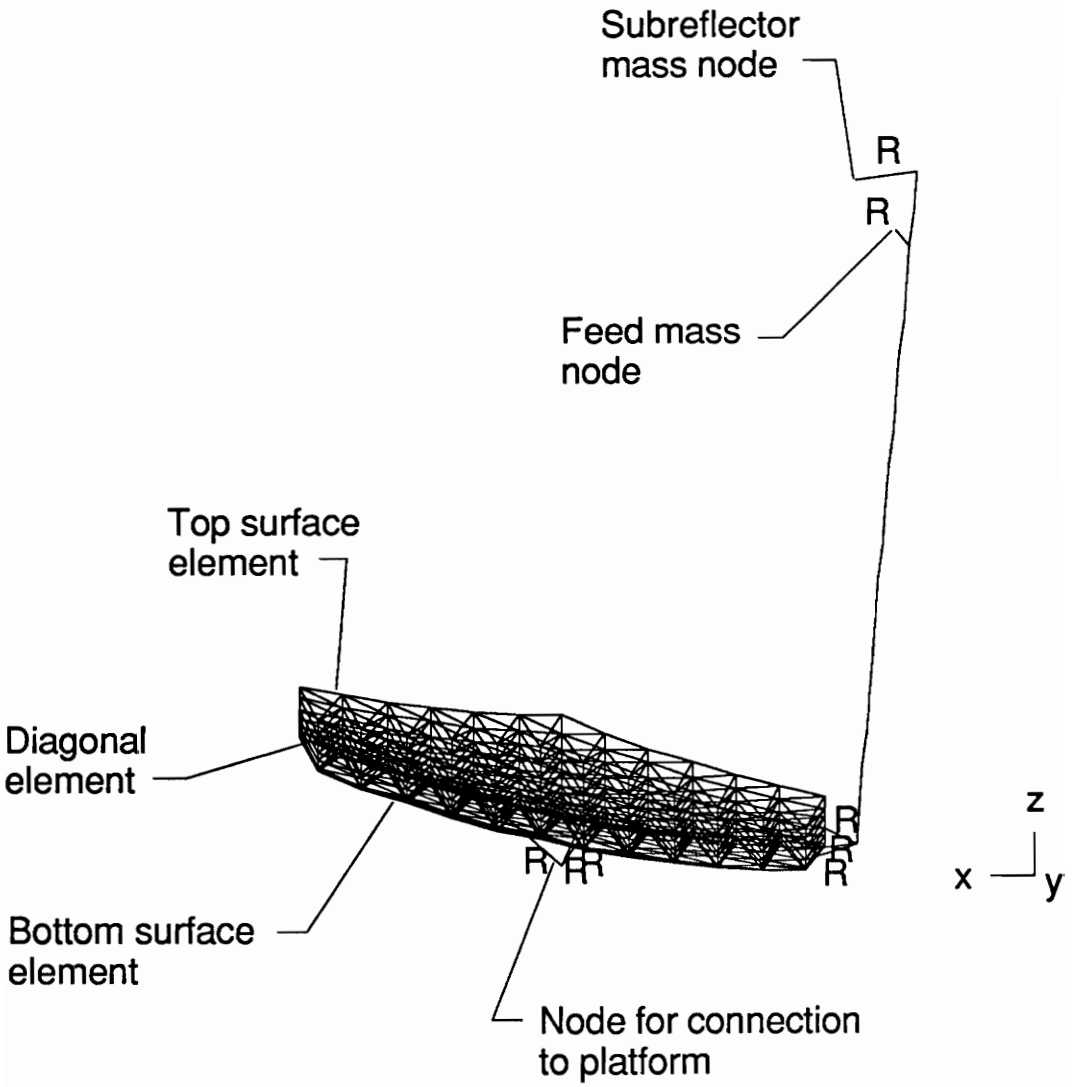

Figure 5. LFMR finite-element model. R denotes a rigid bar.

Table 2. Strongback element properties.

	Diagonal elements	Top and bottom surface elements
Young's modulus, N/m^2	1.38×10^{11}	1.38×10^{11}
Poisson's ratio	0.29	0.29
Mass density, kg/m^3	1.52×10^{3}	1.52×10^{3}
Cross-sectional area, m^2	3.35×10^{-5}	4.88×10^{-5}
Moment of inertia of cross section, $kg\text{-}m^2$	1.93×10^{-9}	2.73×10^{-9}
Torsional constant, $kg\text{-}m^2$	3.86×10^{-9}	5.47×10^{-9}
Outer diameter, cm	2.22	2.22
Thickness, mm	0.48	0.70
Average length, cm	118	150

portion of the membrane distributed mass. The beam elements connecting the nodes represent the strut tubes of the strongback truss.

Feed Mast

The feed mast used for this analysis is based on the Minimast truss [32] developed at LaRC as a ground test article to characterize the structural behavior and control of large space structures. It is used in this study because of its known structural characteristics. The Minimast is a deployable, retractable, triangular linear truss constructed of graphite/epoxy composite tubes with aluminum alloy hinges and end fittings. The LFMR feed mast (illustrated in Figure 3) attaches to the reflector strongback at one end and supports the subreflector 19.5 m above the vertex of the parent paraboloid at the other end and the feed system 17.5 m above the vertex of the parent paraboloid. (See Figure 4.)

An equivalent beam structural model of the Minimast was developed for use in this study to reduce the number of degrees of freedom (DOF) in the already complex LFMR model. The beam model of the feed mast was verified by comparison with a detailed truss mast model. The physical and material properties of the equivalent beam structural model are shown in Table 3. The feed mast model is composed of 18 beam elements (each representing a bay of Minimast truss) and 19 nodes (each supporting a lumped mass element representing the appropriate mass and torsional inertia of the hinges and connectors between each truss bay). The mast is connected to the primary reflector via three rigid bars (indicated by "R" in Figure 5).

Table 3. Structural characteristics of Minimast equivalent beam model.

Beams

Axial stiffness, N	1.15×10^8
Bending stiffness, N-m^2.	1.22×10^7
Torsional stiffness, N-m^2.	1.10×10^6
Mass per unit length, kg/m	4.8

Lumped masses	**End nodes**	**Interior nodes**
Mass, kg	2.33	2.33
Torsional inertia, kg-m^2	1.48	1.76

Subreflector

The subreflector size, which was determined from Cassegrain antenna geometry, was based on the following: (1) the height of the subreflector above the primary reflector in the direction of the primary-reflector parent-paraboloid axis of symmetry (19.5 m), and (2) the offset distance of the primary reflector from the vertex of its parent paraboloid (Figure 4). The resulting subreflector was determined to be 2.35 m in diameter. Since a high-precision subreflector surface will be required for the operating frequencies of the LFMR, the surface was assumed to be constructed of solid panel segments supported by a tetrahedral truss strongback, similar to those under current study as a part of the Precision Segmented Reflector (PSR) program [33]. An areal density of 12 kg/m^2 was assumed for the panels and strongback, resulting in a subreflector mass of 52 kg.

For the structural model, the subreflector is approximated as a lumped mass element concentrated at a single node with its inertias computed as for a right circular cylinder with the above dimensions and mass. It is attached to the feed mast via a rigid bar connection (indicated by "R" in Figure 5) at 19.5 m above the vertex of the parent paraboloid.

Feed System

Since the details of the feed system design are not yet known, approximate calculations were used to determine a representative feed system for incorporation in the LFMR model. The mass of the feed system is estimated based on that of the scanning feed array of a single-aperture Earth-sensing radiometer feed system described in [34]. This estimate, described in [24], yields a feed mass of 443 kg. Like the subreflector, the

feed array is represented as a lumped mass in the structural model of the antenna system. It is rigidly connected to the feed mast at 17.5 m above the vertex of the parent paraboloid.

Chapter 3. Modal Analysis

Preliminary modal analyses were first performed on the reflector alone and the feed mast alone to serve as a comparison with the complete antenna system. These were performed with free-free (unrestrained) boundary conditions resulting in fundamental frequencies of 14.06 and 2.18 Hz, respectively. The LFMR was then analyzed in two configurations, the free-flyer antenna and the platform-mounted antenna, as described below. Each configuration was solved free-free for the first 15 natural modes. Because of the free-free boundary conditions, the first six modes in each case are the six rigid-body modes which correspond to the six degrees of freedom (three translational and three rotational). The rigid-body modes do not contribute to the vibrational response of the system. Rigid-body motion could be induced by various on-orbit disturbances, including those described in this report; however this is an overall spacecraft control issue, not an antenna performance issue. It was therefore assumed for the present study that an adequate attitude control subsystem exists to maintain the desired spacecraft position and orientation.

Free-Flyer Antenna

It has been suggested that the LFMR be flown aboard its own dedicated spacecraft because of its large size and mass. The complete antenna was therefore analyzed in a free-free configuration to simulate orbiting the LFMR as a free flyer (i.e., on a dedicated spacecraft) with the assumption that the supporting subsystem masses are negligible compared with the mass of the antenna.

Use of the flexible feed mast to attach the massive subreflector and feed system to the more massive primary reflector dramatically lowers the structural frequencies of the

overall antenna system from that of either the reflector or the feed mast alone. The rigid connection between the dish and feed mast acts to cantilever the mast to the reflector, thus resulting in the lower fundamental frequency of 1.38 Hz for the overall system, which corresponds to a feed mast bending mode shape as expected. Figures 6-14 illustrate the first nine mode shapes for the free-flyer antenna, and Table 4 lists their corresponding natural frequencies along with a brief description of each mode shape. For clarity, the distortions are greatly exaggerated and only the elements that comprise the strongback top surface (where the membrane is attached), the feed mast, and the rigid bar connector to the subreflector are shown in all mode shape Figures. Both the mode shapes (solid lines) and the undeformed geometries (dashed lines) are shown.

In general, the free-flying configuration has mode shapes that exhibit rotation of both the feed beam and the reflector about the point where they are rigidly connected. An inspection of the lower flexible body mode shapes suggests that modes 2 and 3 are most likely to contribute to pointing errors about the x-axis. Pointing errors about the y-axis include modes 1 and 4. The mode shapes that may contribute to the defocus of the antenna include modes 1 and 4. Contributions may also be made by higher-order modes; however, these will be less significant than those of the lower-order modes. Surface roughness is probably induced by combinations of all the dynamic modes, since they all exhibit distortions to the optimum paraboloidal shape, with the lower-order modes being the primary contributors.

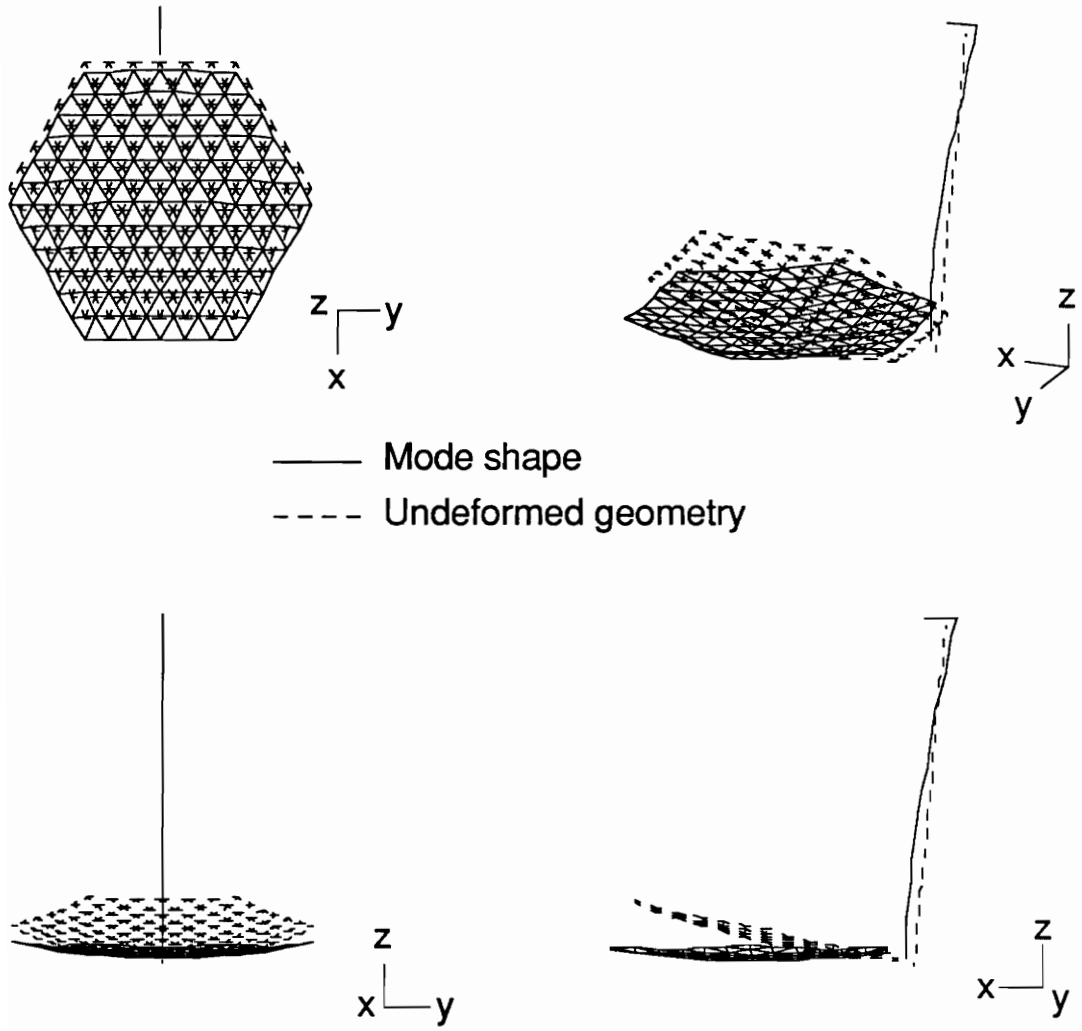

Figure 6. Mode 1 for free-flyer antenna. f_n = 1.38 Hz.

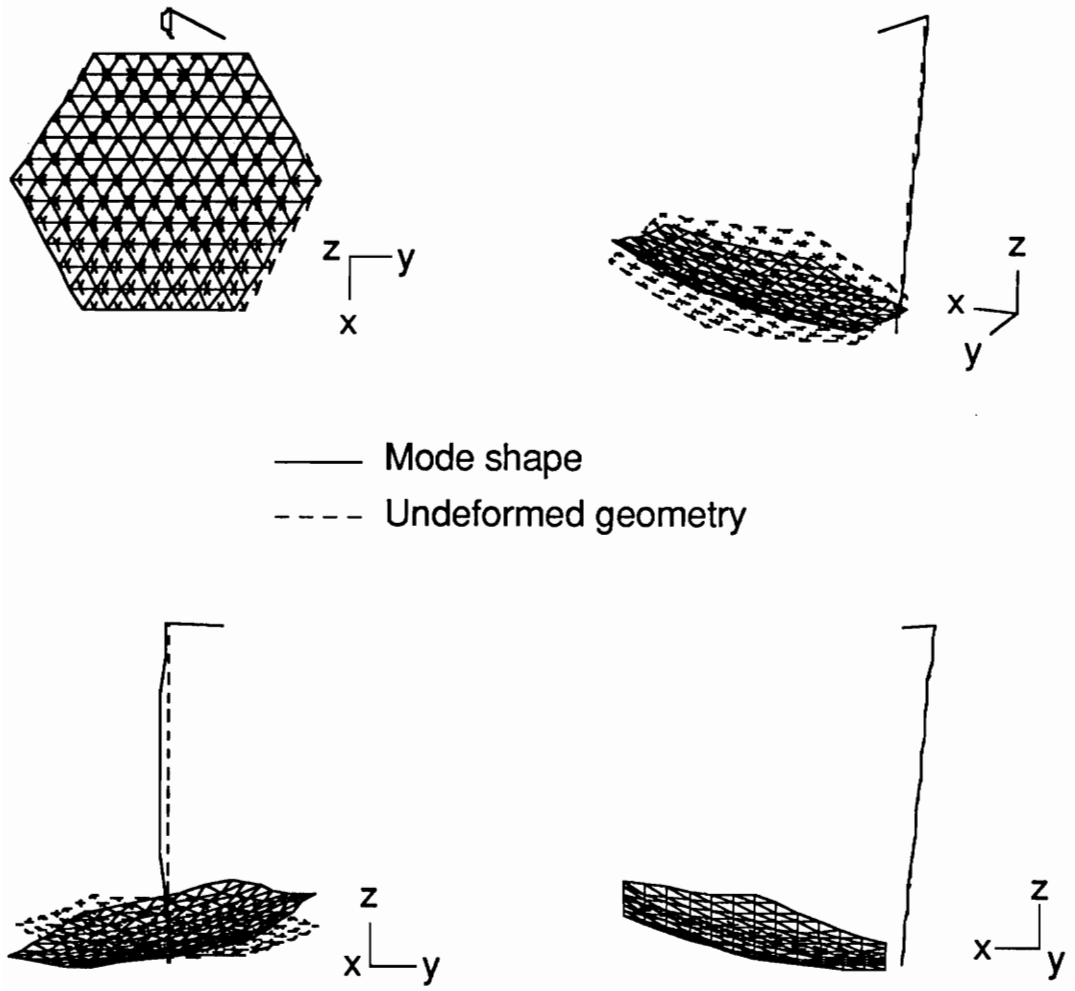

Figure 7. Mode 2 for free-flyer antenna. f_n = 2.30 Hz.

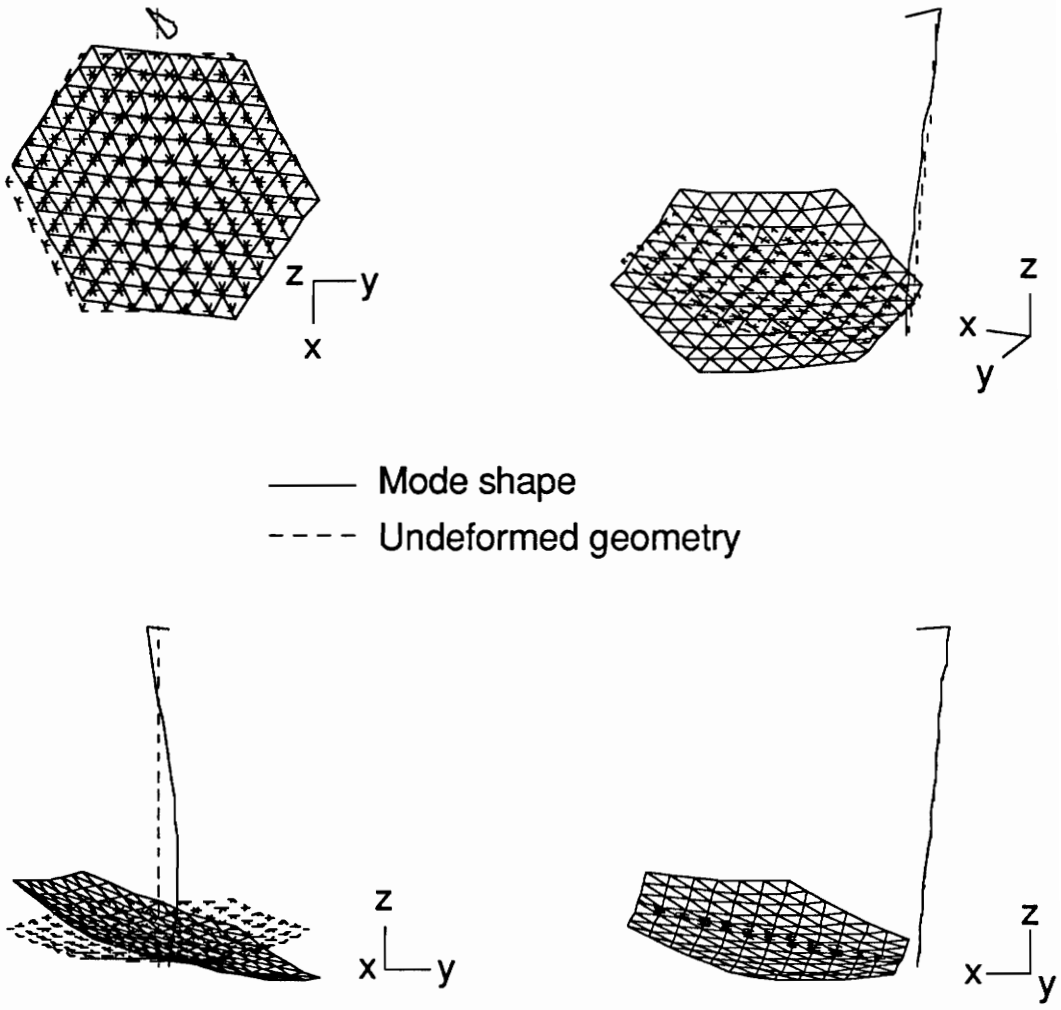

Figure 8. Mode 3 for free-flyer antenna. f_n = 2.81 Hz.

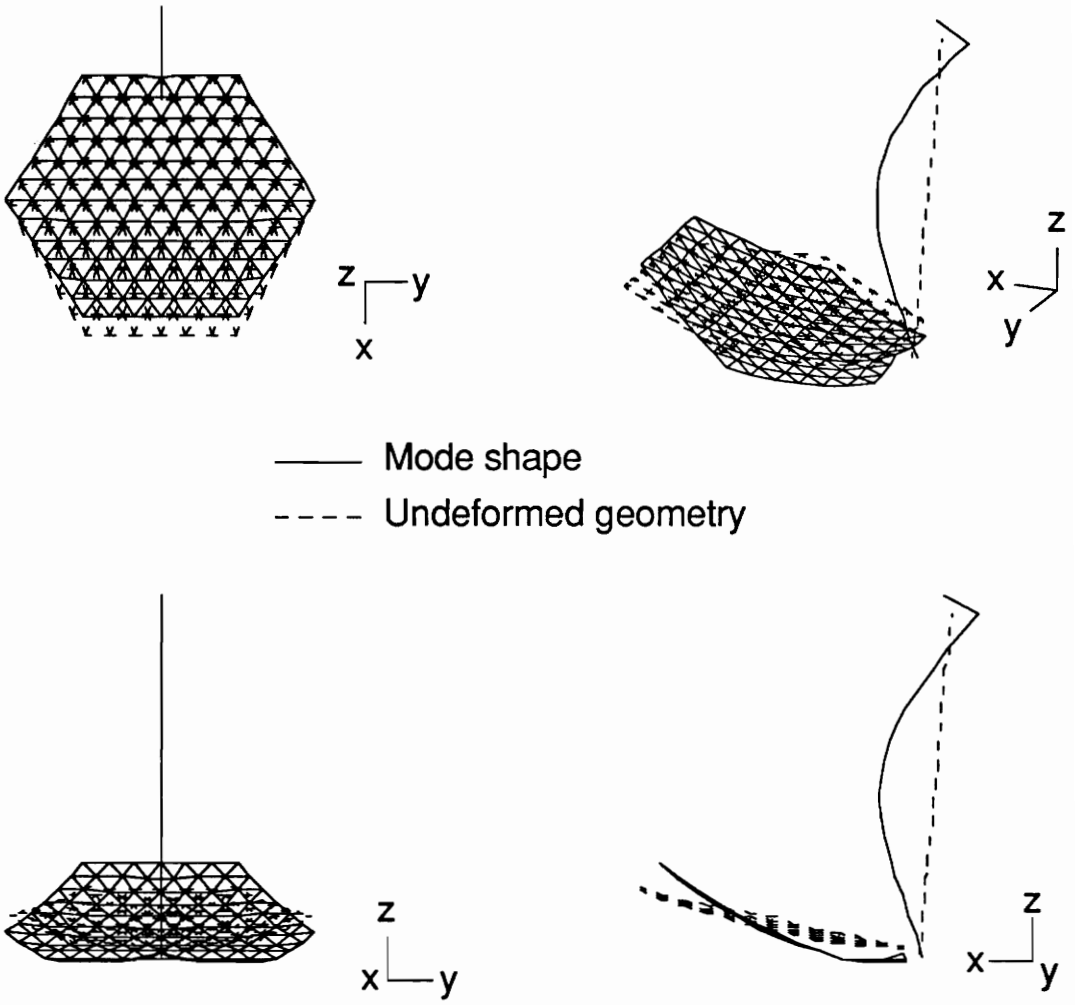

Figure 9. Mode 4 for free-flyer antenna. f_n = 7.48 Hz.

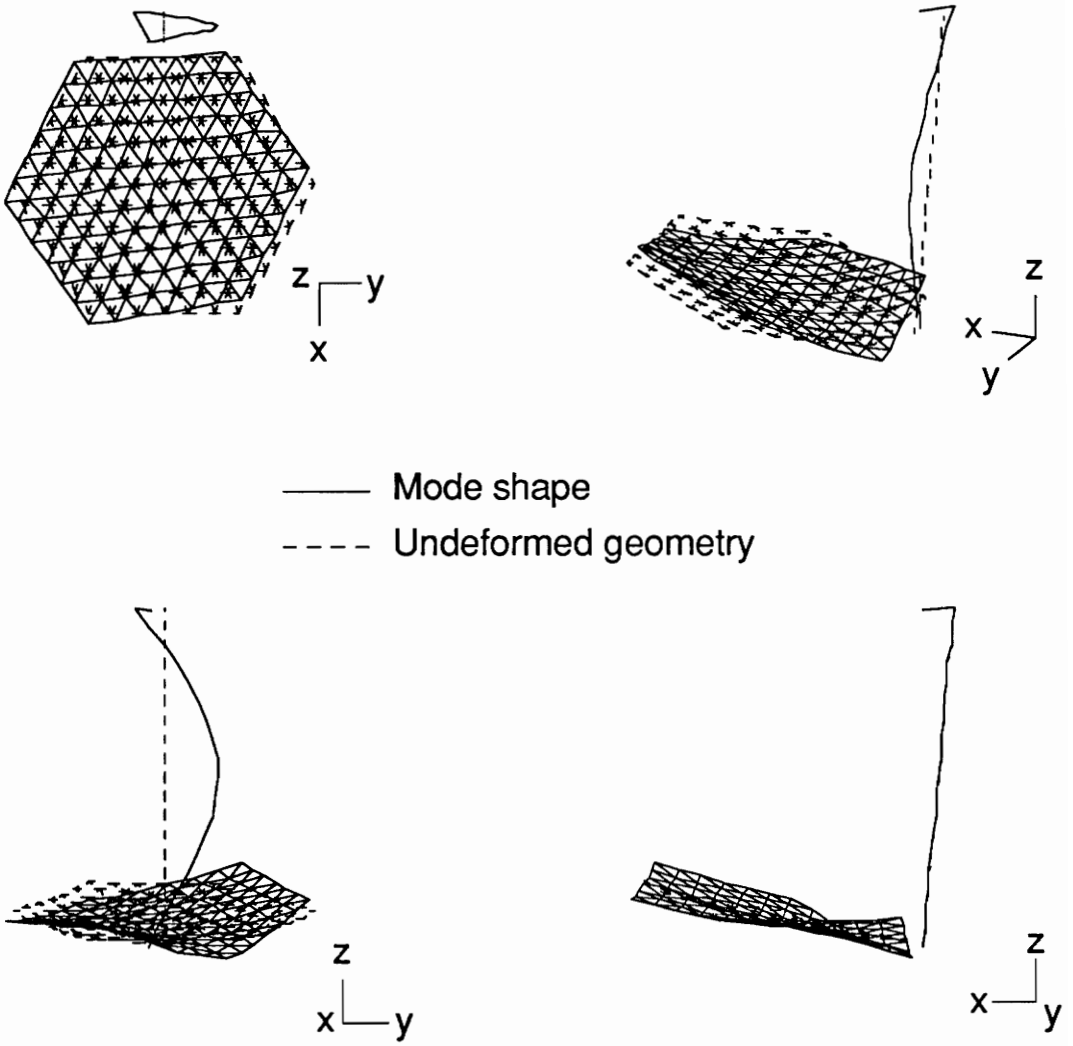

Figure 10. Mode 5 for free-flyer antenna. $f_n = 9.44$ Hz.

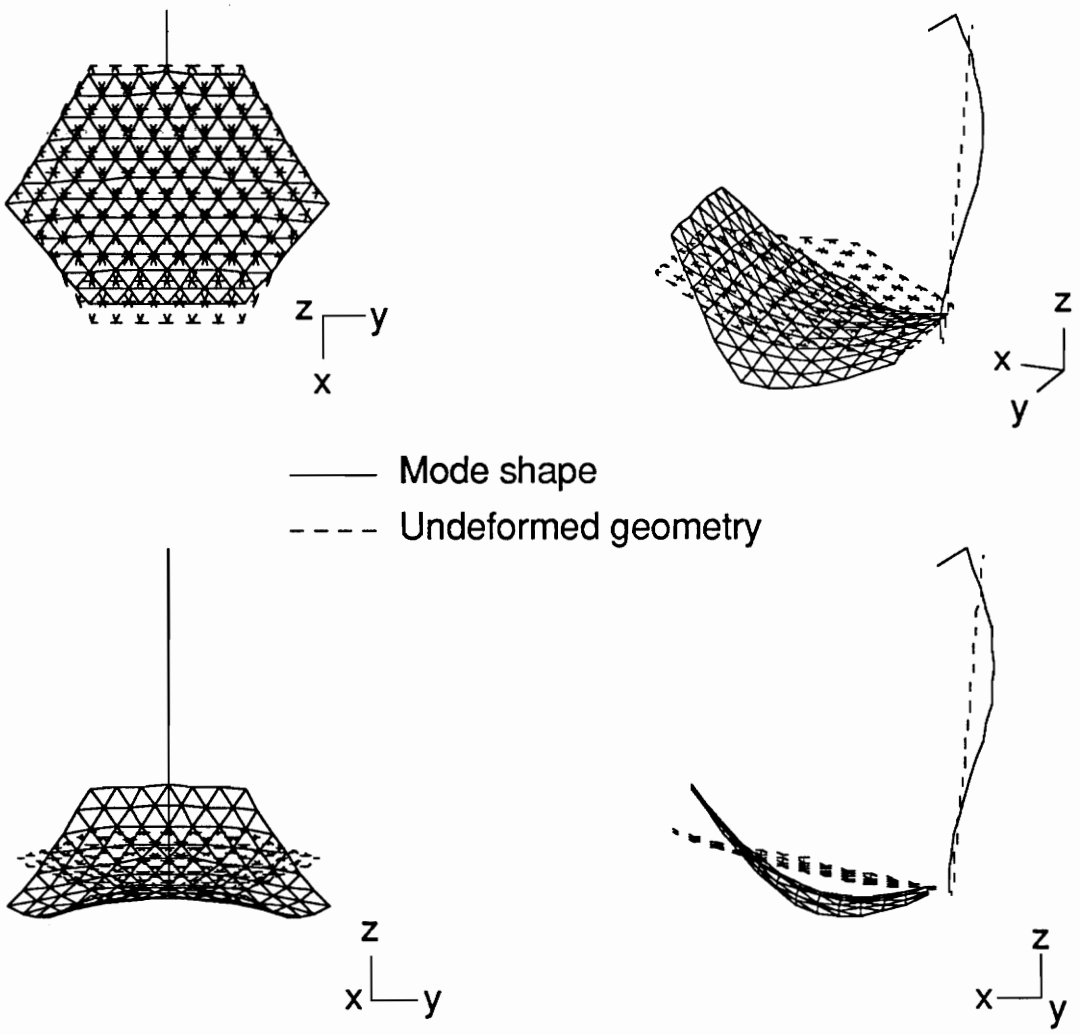

Figure 11. Mode 6 for free-flyer antenna. f_n = 10.98 Hz.

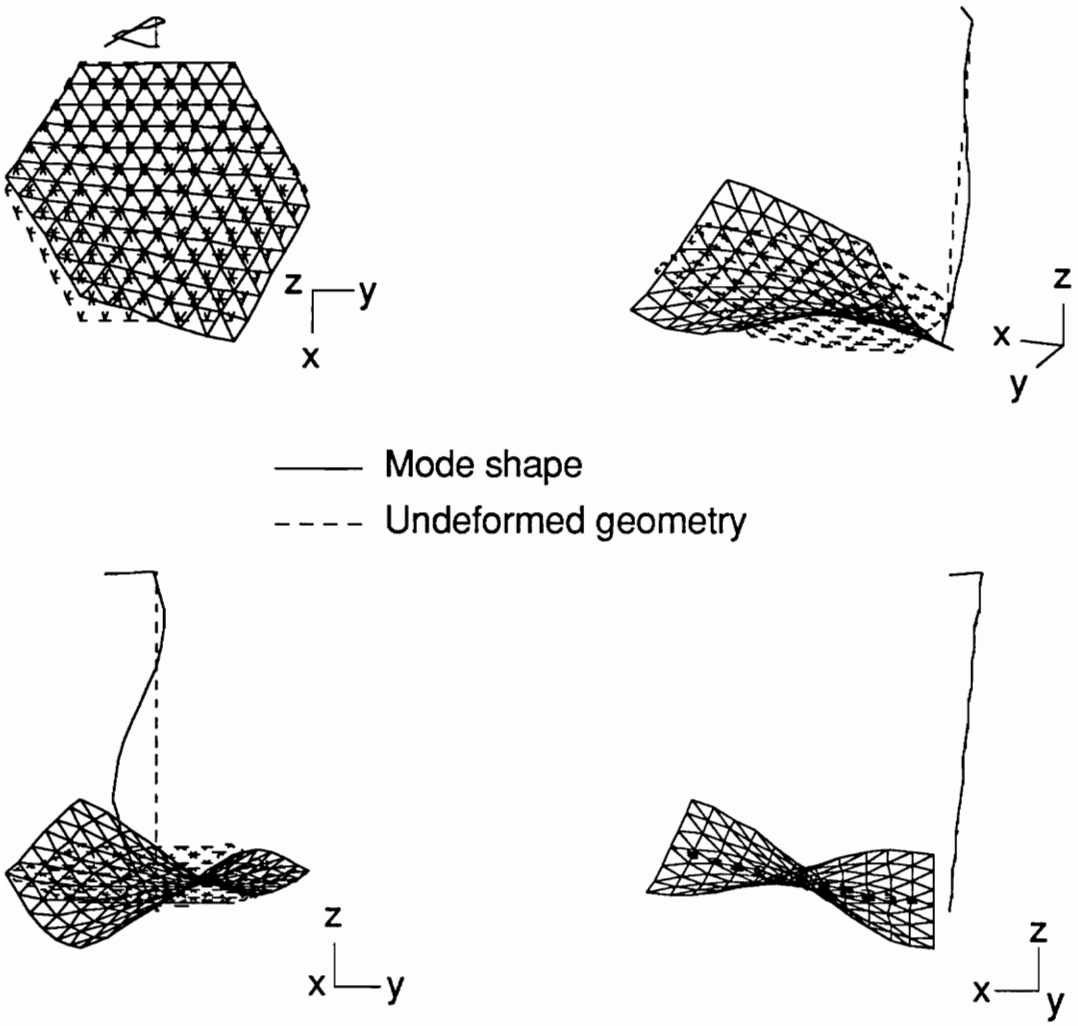

Figure 12. Mode 7 for free-flyer antenna. f_n = 14.27 Hz.

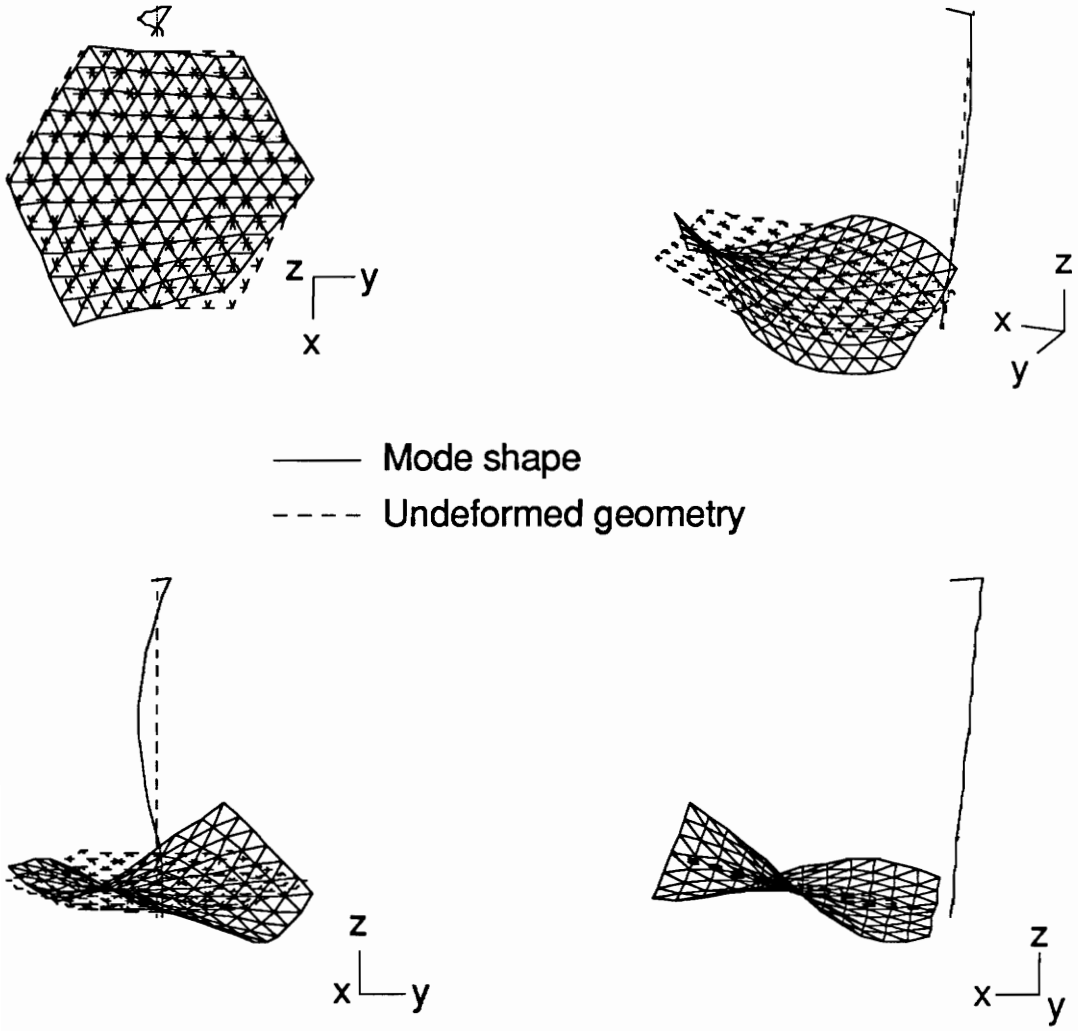

Figure 13. Mode 8 for free-flyer antenna. f_n = 16.65 Hz.

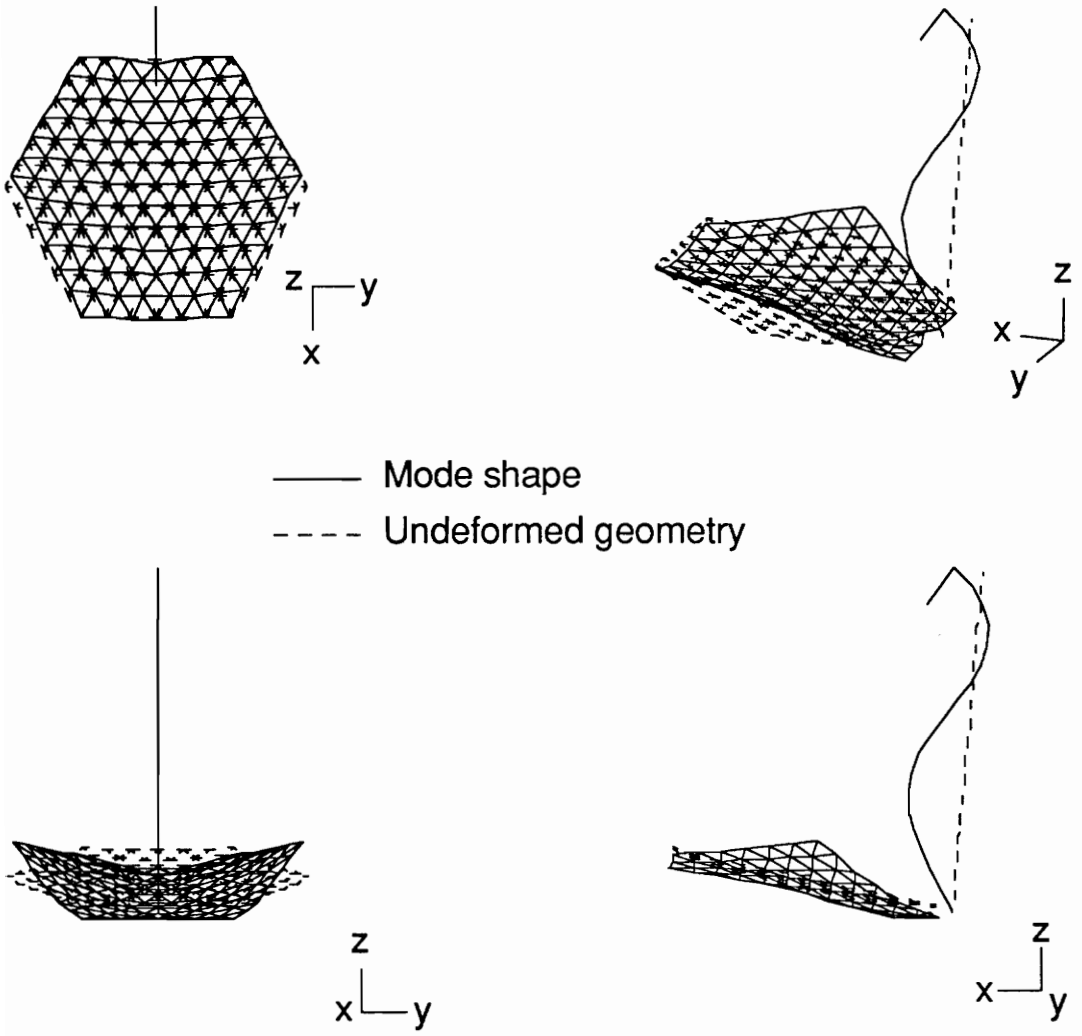

Figure 14. Mode 9 for free-flyer antenna. f_n = 18.00 Hz.

Table 4. Natural frequencies of free-flyer LFMR.

Flexible mode	Natural frequency, Hz	Description of mode shape
1	1.382	Reflector rocking and mast bending about y
2	2.302	Reflector rocking about x and mast twisting about z
3	2.807	Reflector rocking and mast bending about x
4	7.479	Reflector and mast bending about y
5	9.440	Reflector torsion about x and mast bending about x
6	10.98	Reflector and mast bending about y
7	14.27	Reflector torsion about x and mast bending about x
8	16.65	Reflector torsion about x and mast bending about x
9	18.00	Reflector bending about x and mast bending about y

Platform-Mounted Antenna

Next, the antenna was rigidly attached at three central nodes on the bottom of the strongback to the geostationary platform, which is represented as a lumped mass with appropriate mass properties as listed in Table 5. (See Figure 5.) This platform-mounted configuration was also analyzed under free-free conditions. In this configuration the effects of the mass and inertia of the platform are considered but its elastic properties are not. The resulting natural frequencies and mode shape descriptions are listed in Table 6, with the mode shapes illustrated in Figures 15-23. Connecting the LFMR to the considerably greater mass and inertia of the platform lumped mass acts to nearly cantilever the entire antenna at the connection region, thus yielding a structure with natural frequencies much lower than those of the free-flyer case.

The mode shapes seen for this case appear somewhat similar to those of the free-flyer case, however the rigid connection of the reflector and the platform mass, coupled with the relatively large inertia of the platform about the y-axis (see Figure 1), yields a cantilever-like condition about the y-axis for the entire antenna system. This causes several general differences between the corresponding mode shapes of the two configurations, which are discussed below.

The three nodes attached to the platform mass tend to remain relatively fixed, particularly with respect to rotation about the y-axis, which is an axis of large platform inertia. In general, the pointing errors about the y-axis due to the distortion of the surface are therefore expected to be less for the platform-mounted configuration than for the free-flyer configuration. Nearly fixing these three nodes also causes the reflector to move about its own center, i.e., the area of connection to the platform mass, rather than to move about the connection to the feed mast, as was seen in the free-flyer case.

Table 5. Platform lumped mass properties.

Mass, kg	5726
I_{xx}, kg-m^2	7.969×10^4
I_{yy}, kg-m^2	2.961×10^5
I_{zz}, kg-m^2	3.034×10^5
I_{xy}, kg-m^2	3.635×10^2
I_{yz}, kg-m^2	2.401×10^3
I_{zx}, kg-m^2	3.161×10^4

Table 6. Natural frequencies of platform-mounted LFMR.

Flexible mode	Natural frequency, Hz	Description of mode shape
1	0.4461	Mast bending about y
2	0.7196	Reflector rocking and mast bending about x
3	2.100	Reflector rocking and mast bending about y
4	2.332	Mast twisting about z
5	6.892	Reflector rocking and mast bending about x
6	7.909	Reflector rocking and mast bending about y
7	8.816	Reflector torsion about x and mast bending about x
8	10.50	Reflector and bending about y
9	13.94	Reflector twisting about z and mast bending about x

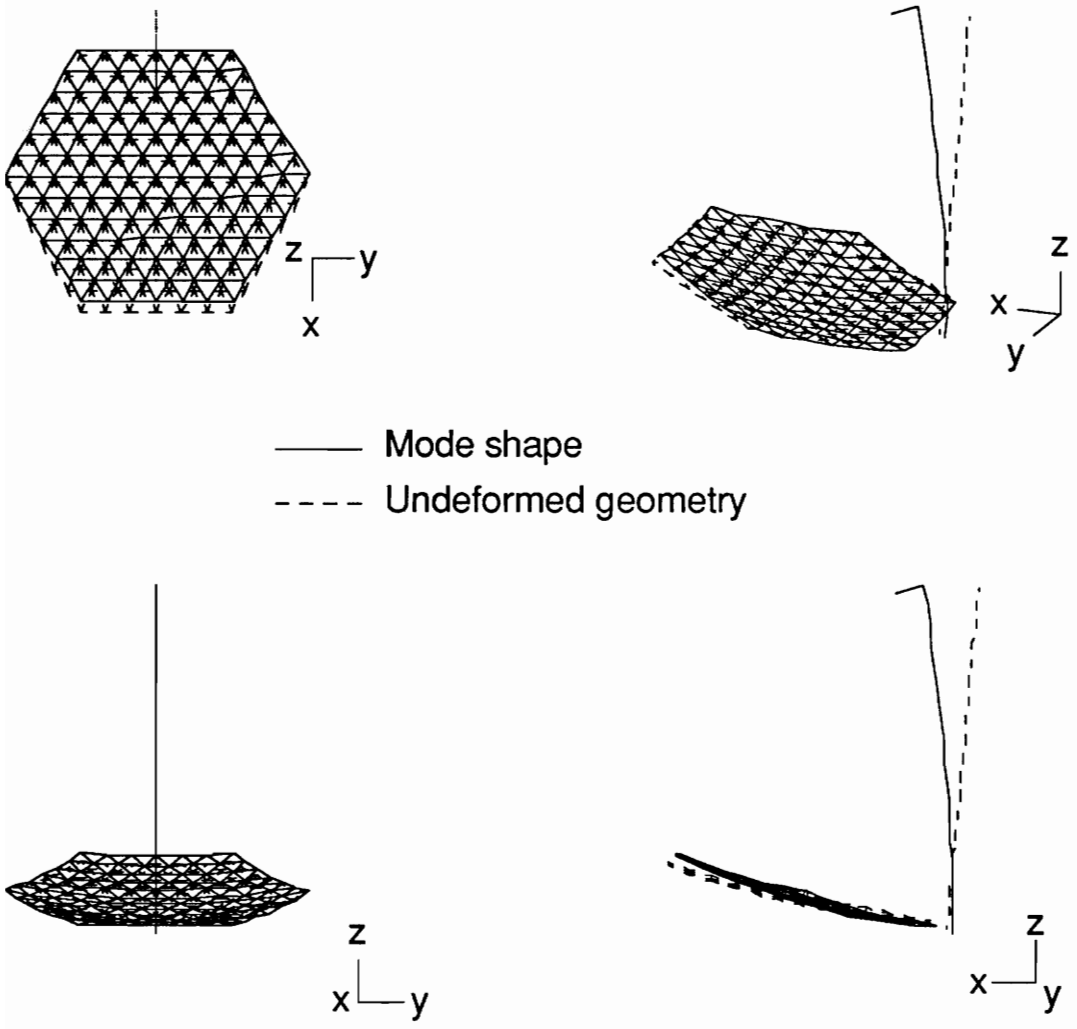

Figure 15. Mode 1 for platform-mounted antenna. f_n = 0.45 Hz.

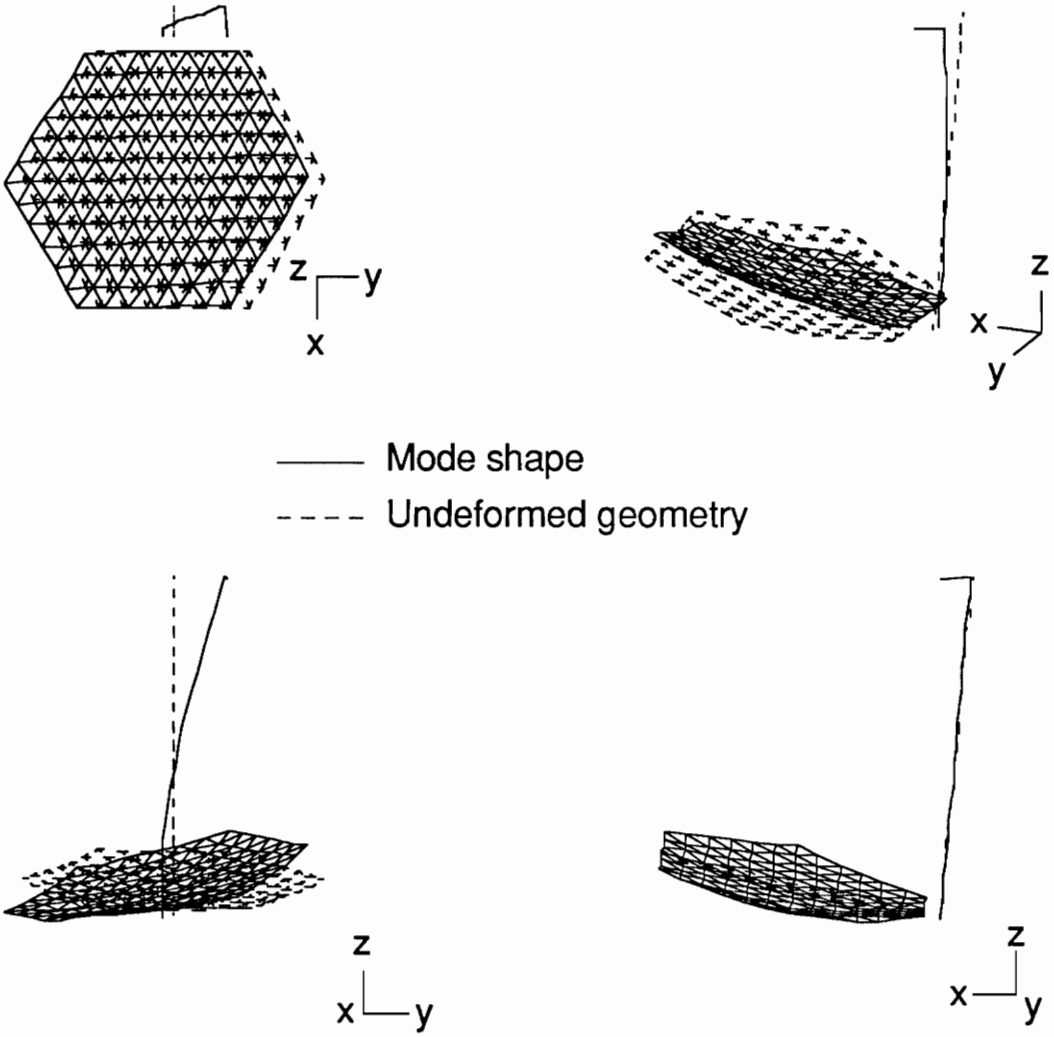

Figure 16. Mode 2 for platform-mounted antenna. $f_n = 0.72$ Hz.

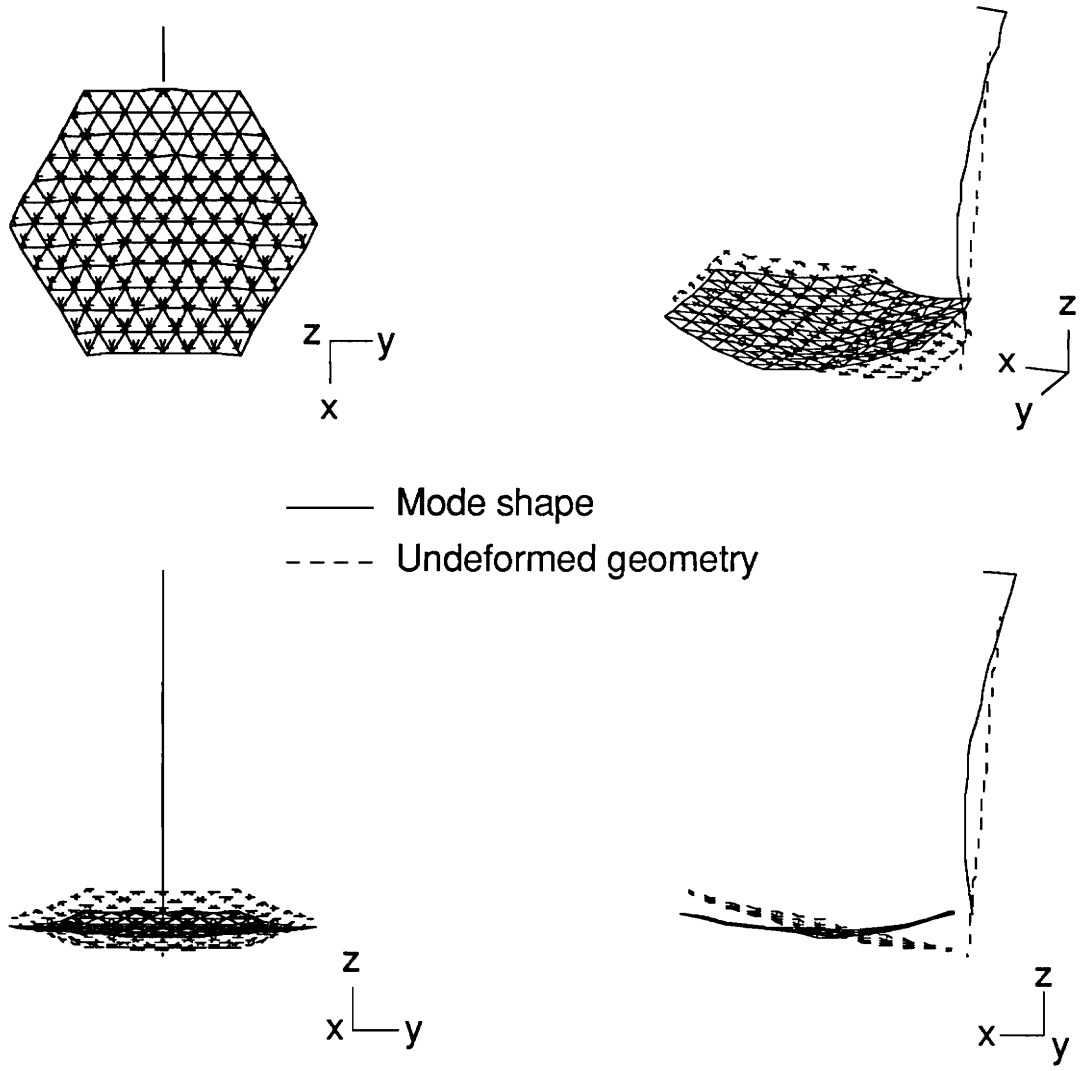

Figure 17. Mode 3 for platform-mounted antenna. f_n = 2.10 Hz.

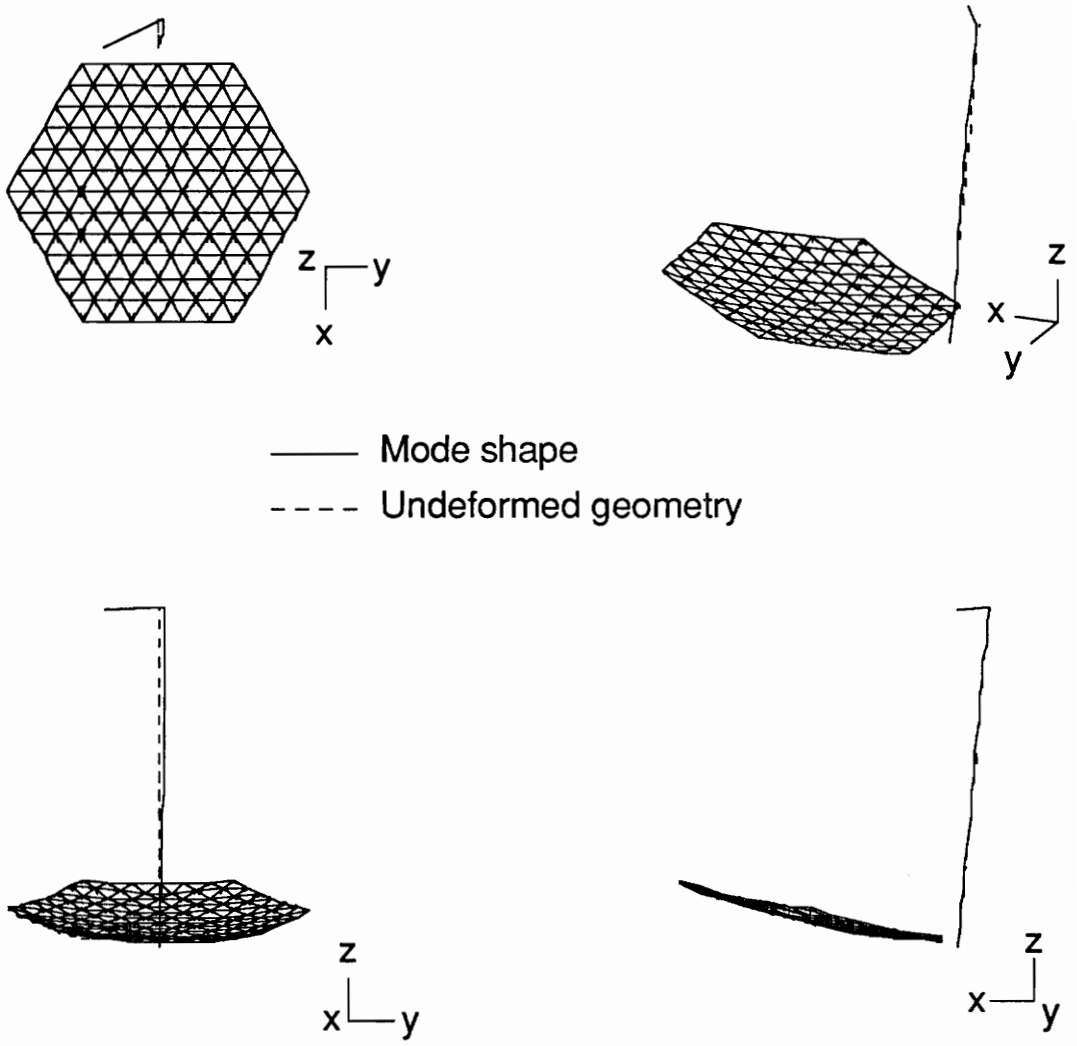

Figure 18. Mode 4 for platform-mounted antenna. f_n = 2.33 Hz.

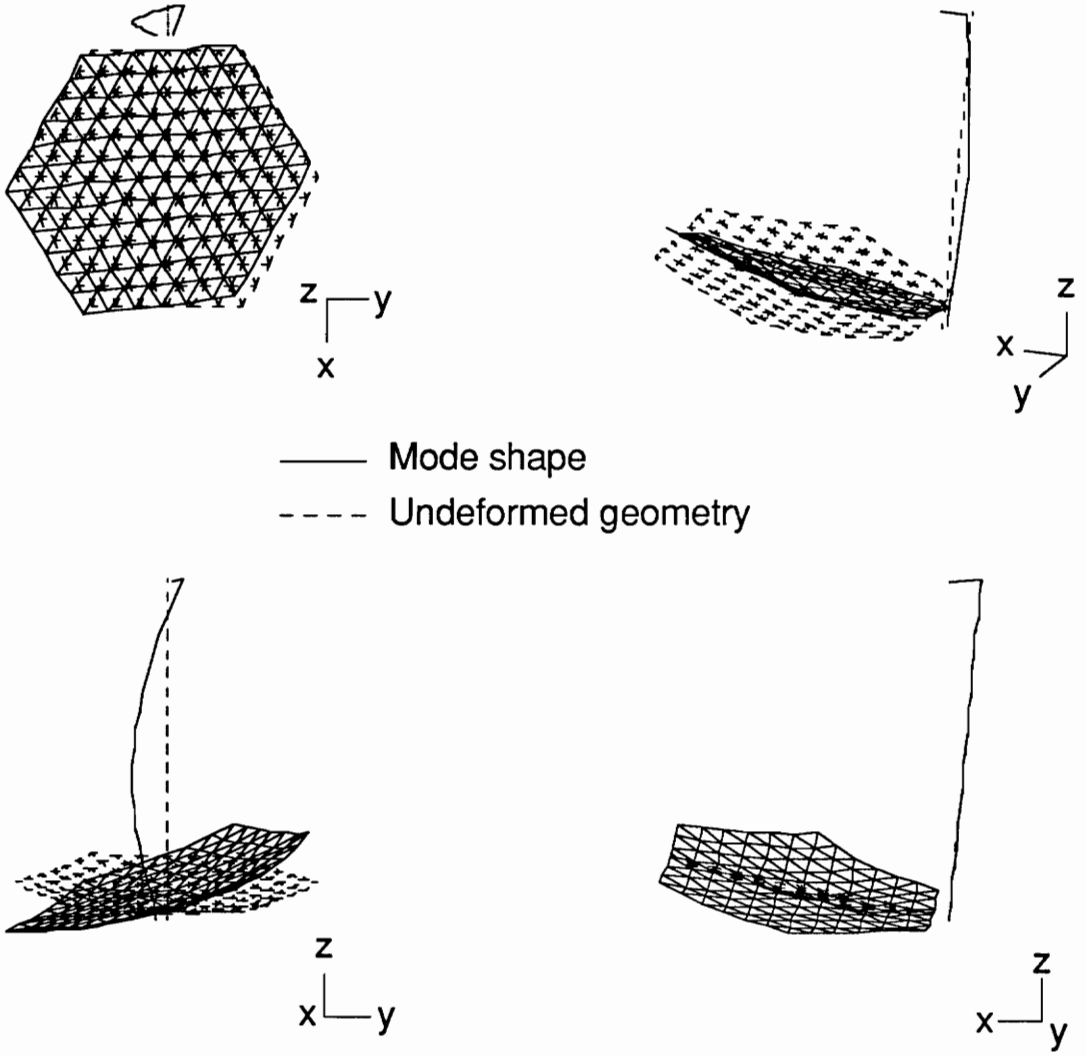

Figure 19. Mode 5 for platform-mounted antenna. f_n = 6.89 Hz.

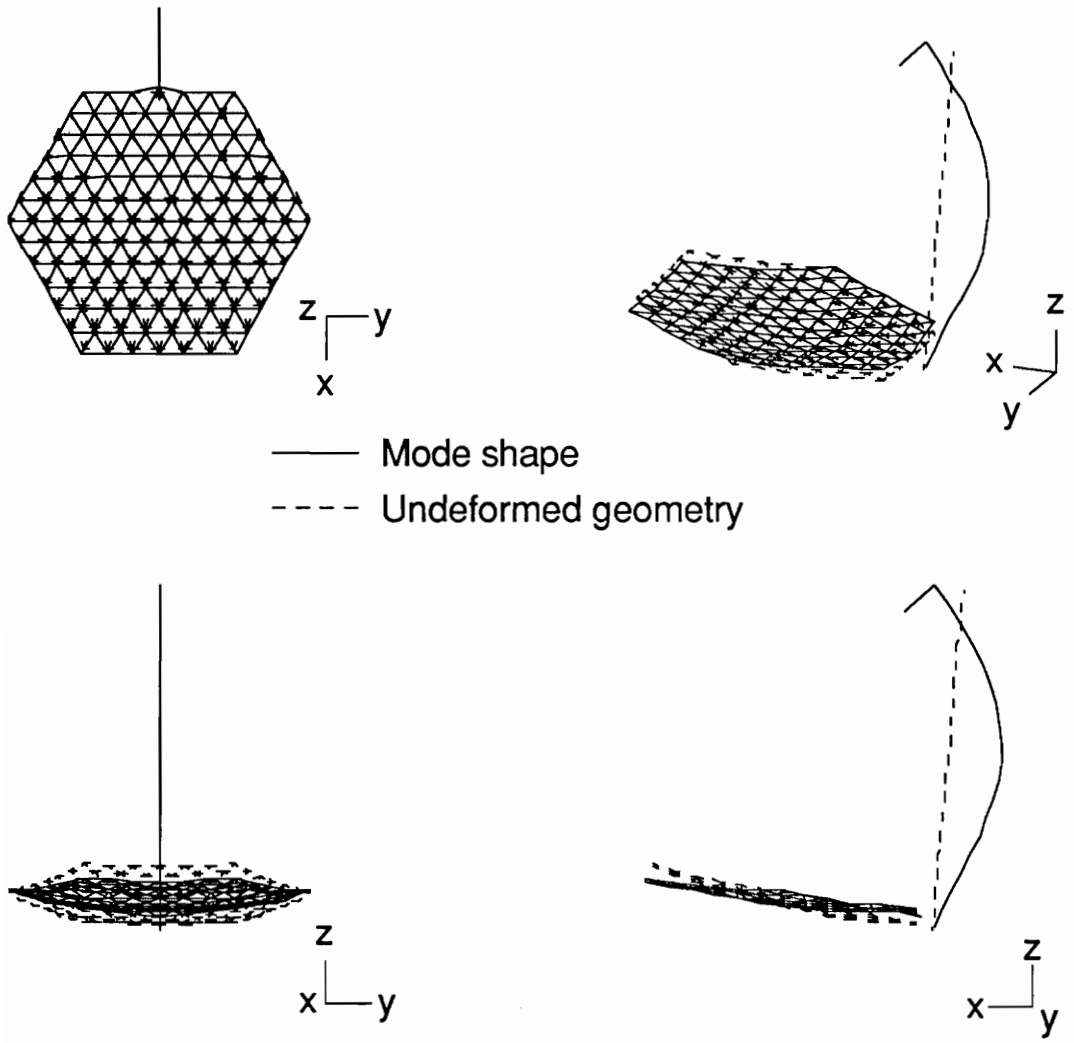

Figure 20. Mode 6 for platform-mounted antenna. f_n = 7.91 Hz.

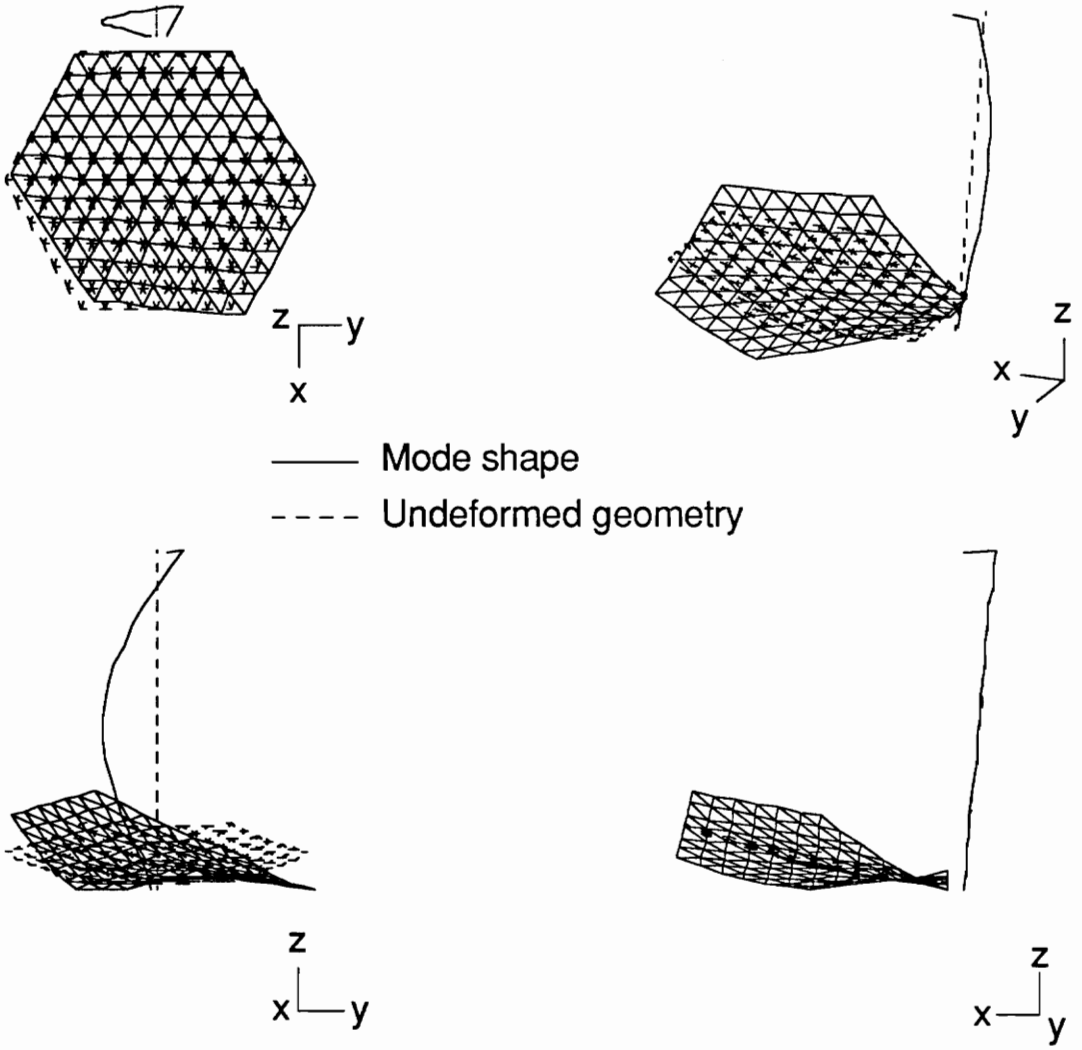

Figure 21. Mode 7 for platform-mounted antenna. f_n = 8.82 Hz.

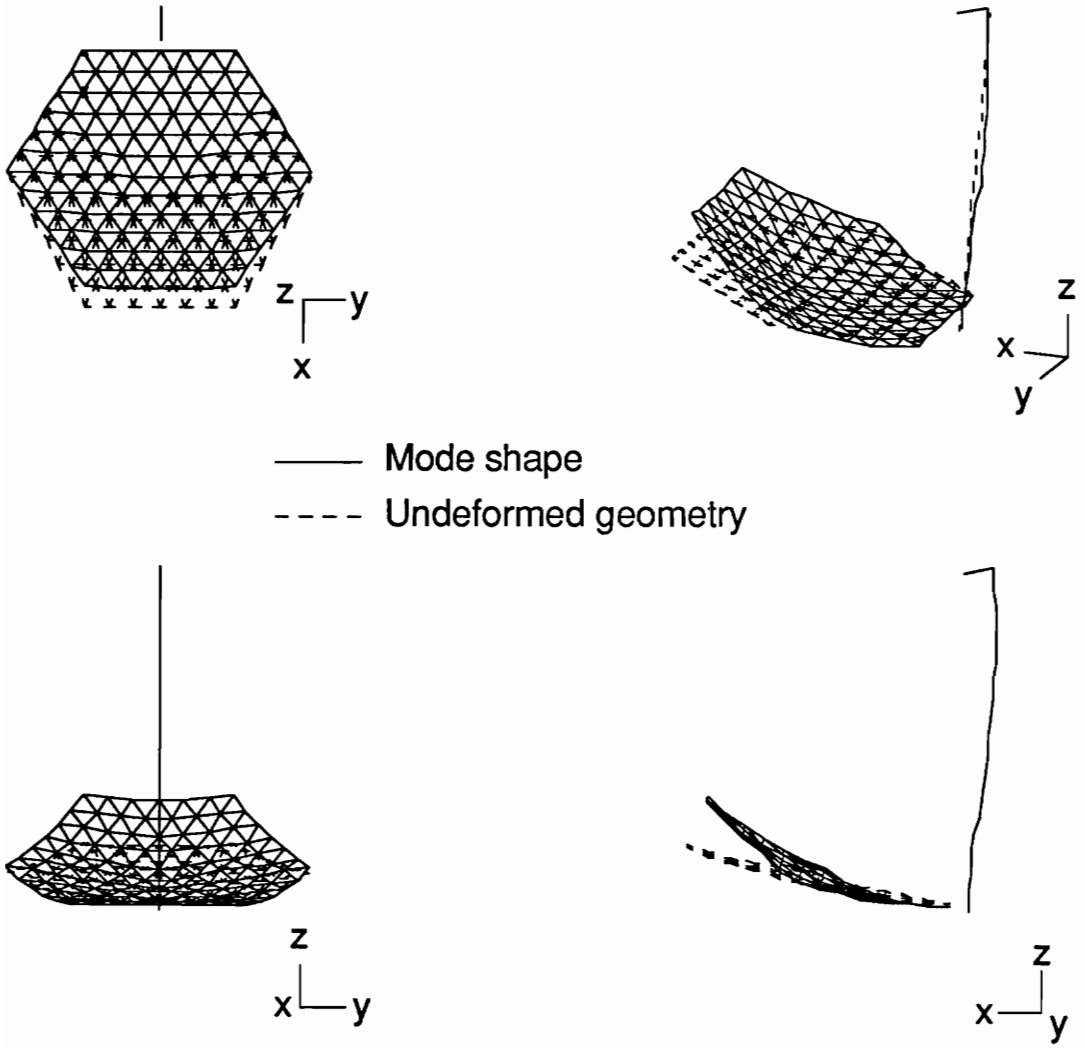

Figure 22. Mode 8 for platform-mounted antenna. f_n = 10.50 Hz.

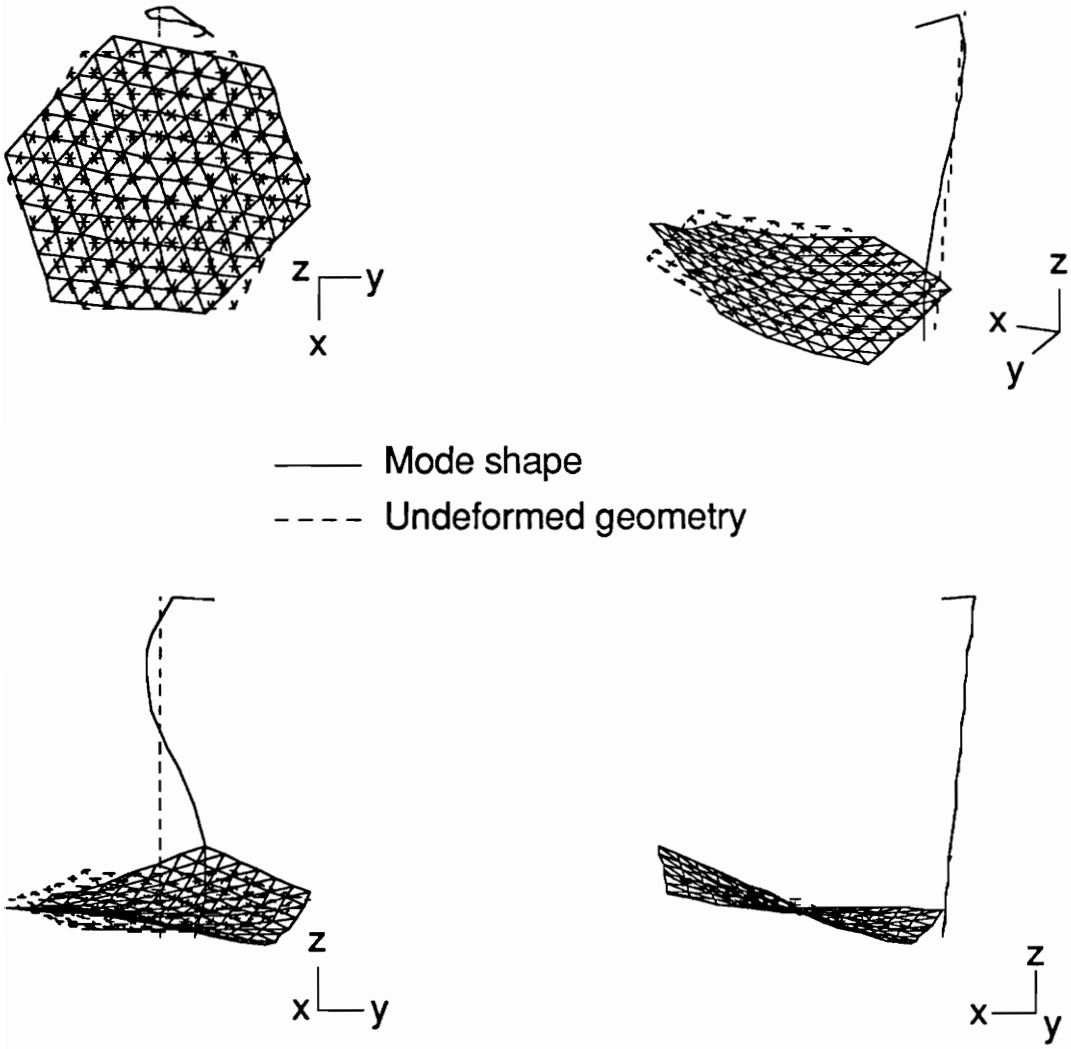

Figure 23. Mode 9 for platform-mounted antenna. f_n = 13.94 Hz.

An inspection of the mode shapes indicates that modes 2 and 4 are probably the lower-order modes that contribute to pointing errors about the x-axis. The y-axis pointing error modes include modes 1 and 3. Those that may contribute to the defocus of the antenna include modes 1 and 3. As in the free-flyer case, surface roughness errors appear to be induced by combinations of all the dynamic modes, particularly the lower-order modes.

Chapter 4. On-Orbit Disturbances and Excitation Functions

From its location in geosynchronous orbit, the LFMR will need to scan most of the Earth disk, although the exact scanning operation is undecided at this time. There are a variety of alternatives being examined, including mechanical scanning, electronic scanning, and combinations thereof. The assumption in the present study is that the scanning will be accomplished mechanically, without momentum compensation (for conservatism), by rotating the subreflector about its x- and y-axes for north-south and east-west scanning, respectively. The subreflector motion is one of the primary on-orbit disturbances that could degrade the electromagnetic performance of the antenna by inducing surface roughness, pointing errors, and defocus. A representative onboard disturbance that simulates subreflector scanning was modeled to evaluate the dynamic performance of the LFMR in space. This disturbance consists of two torque input equations representing the orthogonal components of the scan (i.e., subreflector rotation about the x- and y-axes).

Excitation (torque) functions were generated for a representative scanning scenario based on the retrace time (the time allotted for each Earth-disk scan) and the footprint (the projection of the half-power beamwidth on the Earth) requirements. More frequent retraces yield more severe forcing conditions, since the subreflector must be rotated more quickly. Smaller footprints also cause quicker movements and higher accelerations since there are more spots to scan within the allotted retrace time. The retrace time examined was 30 min (1800 s), which is appropriate for a range of proposed science requirements.

The Earth footprint capabilities of the LFMR were found with the following equation [30]:

$$F=1.2H\left(\frac{\lambda}{D}\right)$$

where F is the subsatellite footprint diameter, H is the orbit altitude (H_{GEO} = 35760 km), λ is the wavelength of the operating frequency, and D is the diameter of the antenna primary reflector. The resulting footprints for the various operating frequencies of the 15-m-diameter LFMR are listed in Table 7. In order to provide a conservative disturbance model, a 10-km footprint is assumed for the 30-min retrace time, which may better satisfy the science requirements and is more stringent than the Table 7 values.

The LFMR was assumed to employ a raster-type scan technique. A raster scan is performed by dividing the desired area into a grid of spots with dimensions of the desired resolution and then scanning back and forth line by line across the grid. As shown in Figure 24, the scenario for the LFMR is that a line is scanned from east to west, followed by a north-south step down to the succeeding line, which is then scanned from west to east. This "S" pattern is repeated until the entire area is scanned. The following discussion describes the formulation of the torque functions for the subreflector raster scan.

From geosynchronous orbit, the coverage requirement of $\pm 7.3^{\circ}$ from nadir [35] yields an area of the Earth disk of approximately 9160×9160 km. The required 10-km ground resolution therefore results in 916 lines of 916 footprints each (10×10 km per footprint). The 30-min allotted time is assumed for operational scanning, i.e., not including time for a reset maneuver or for damping out its associated vibrations. The time t_l to scan each line, including turnaround, is therefore the retrace time divided by the number of lines and is given as follows:

$$t_l = \frac{1800 \text{ s}}{916 \text{ lines}}$$

$$= 1.965 \text{ s/line}$$

Table 7: Footprint diameter as a function of operating frequency.

Operating frequency, GHz	Footprint diameter, km
6	143
10	86
18	48
21	41
37	23

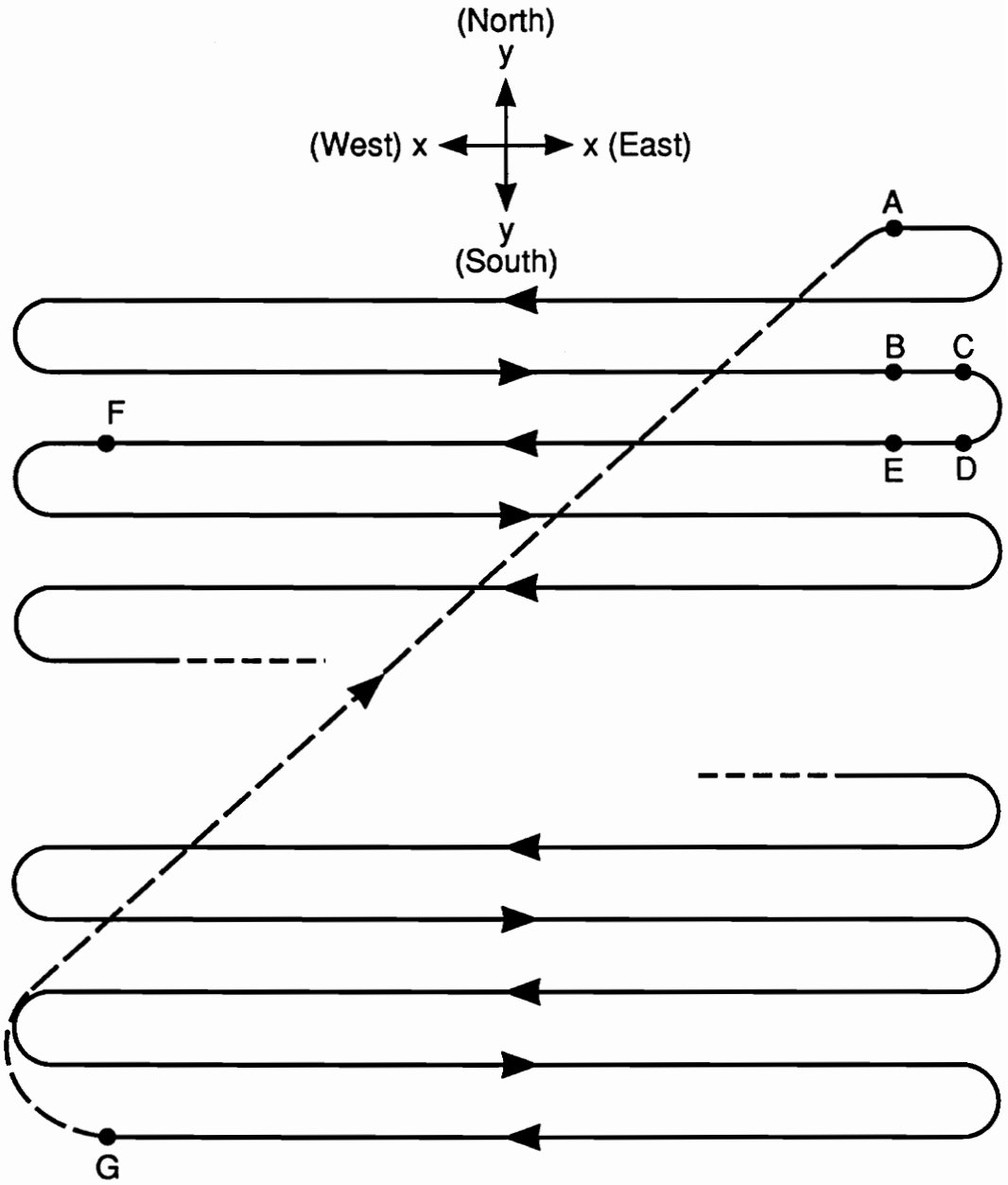

A to G - Full Earth-disk scan
B to F - Individual line scan (duration = t_l)
B to E - East-west turnaround (duration = t_{TA})
C to D - North-south step (duration = t_S)
E to F - Steady motion; no torque (duration = $t_l - t_{TA}$)
G to A - Reset maneuver (duration = t_l)

Figure 24. Antenna scan pattern (not to scale).

The time t_l required for a line scan occurs between points B and F in Figure 24. Note that the frequency of the line scans ($f_l = 1/t_l$) is 0.509 Hz, which is quite close to the first fundamental frequency of the platform-mounted configuration (0.45 Hz). Operating near a resonant condition increases the conservative nature of the scan disturbance model.

East-West Scan

The average east-west scan rate of the beam $\omega_{y,\text{beam}}$ is

$$\omega_{y,\text{beam}} = \frac{14.6 \text{ deg/line}}{1.965 \text{ s/line}}$$

$$= 7.431 \text{ deg/s}$$

Because of the Cassegrain configuration, the beam emitted by the antenna is displaced twice the angle of the subreflector rotation. The required subreflector average scan rate is therefore

$$\omega_{y,\text{av}} = \frac{7.431 \text{ deg/s}}{2}$$

$$= 3.716 \text{ deg/s}$$

which is the scan rate assumed for the steady east-west portion of each scan line.

The time for turnaround t_{TA} is assumed to be 10 percent of the total line time. (In Figure 24, t_{TA} = 0.1965 s from point B to point E.) During this time, the subreflector

must decelerate about the y-axis from $\omega_y = 3.716$ deg/s to zero, displace a north-south step about the y-axis, and accelerate about the y-axis in the negative direction to $\omega_y = -3.716$ deg/s. The angular velocity about the y-axis of the turnaround maneuver is assumed to be a cosine wave of the following form:

$$\omega_y = 3.716 \cos(\frac{\pi t}{0.1965}) \text{ deg/s}$$

The acceleration function is

$$\dot{\omega}_y = -59.416 \sin(\frac{\pi t}{0.1965}) \text{ deg/s}^2$$

The corresponding input torque disturbance function is therefore

$$M_y = 18.623 \sin(\frac{\pi t}{0.1965}) \text{ N-m} \quad (1)$$

(where $M = -I\dot{\omega}$, $I_{xx} = I_{yy} = 18$ kg-m^2, and degrees are converted to radians). Note that the torque that is input to the antenna system is equal in magnitude but opposite in sign to the torque that causes the subreflector motion.

As defined here, each line of scan begins with $t = 0$ s at the beginning of a turnaround maneuver (point B in Figure 24). The transient torque equation is therefore in effect during each line for the time segment $0 \le t \le 0.1965$ s (Figure 24, point B through point E). There is no east-west torque input while the east-west velocity is a constant $\omega_y = 3.716$ deg/s or $\omega_y = -3.716$ deg/s, as appropriate), which occurs during the rest of the line scan ($0.1965 \le t \le 1.965$, point E to point F). This torque function is applied alternately in the positive and negative sense to simulate the velocities and accelerations due

to the back-and-forth east-west motion. The east-west excitation function is plotted in Figure 25(a).

North-South Step

The north-south step time t_S is assumed to be 25 percent of the turnaround time ($t_S = 0.0491$ s). The step occurs from point C to point D in Figure 24. During this time the subreflector must accelerate about the x-axis from $\omega_x = 0$ deg/s to some value of $\omega_{x,max}$, and then decelerate back to zero. With each step the beam must displace the width of one line (10 km), or 0.016°. This requires a subreflector displacement of 0.008°. Time is adjusted so that $t = 0$ s corresponds with that of the east-west case (i.e., point B of Figure 24), which yields the following assumed cosine form displacement equation during the step-down procedure:

$$\theta_x = 0.004 \cos \left[\frac{\pi(t-0.0737)}{0.0491}\right] \text{ deg}$$

The equations of the angular velocity ω_x and acceleration $\dot{\omega}_x$ for the north-south step are, respectively,

$$\omega_x = -0.2562 \sin \left[\frac{\pi(t-0.0737)}{0.0491}\right] \text{ deg/s}$$

and

$$\dot{\omega}_x = -16.388 \cos \left[\frac{\pi(t-0.0737)}{0.0491}\right] \text{ deg/s}^2$$

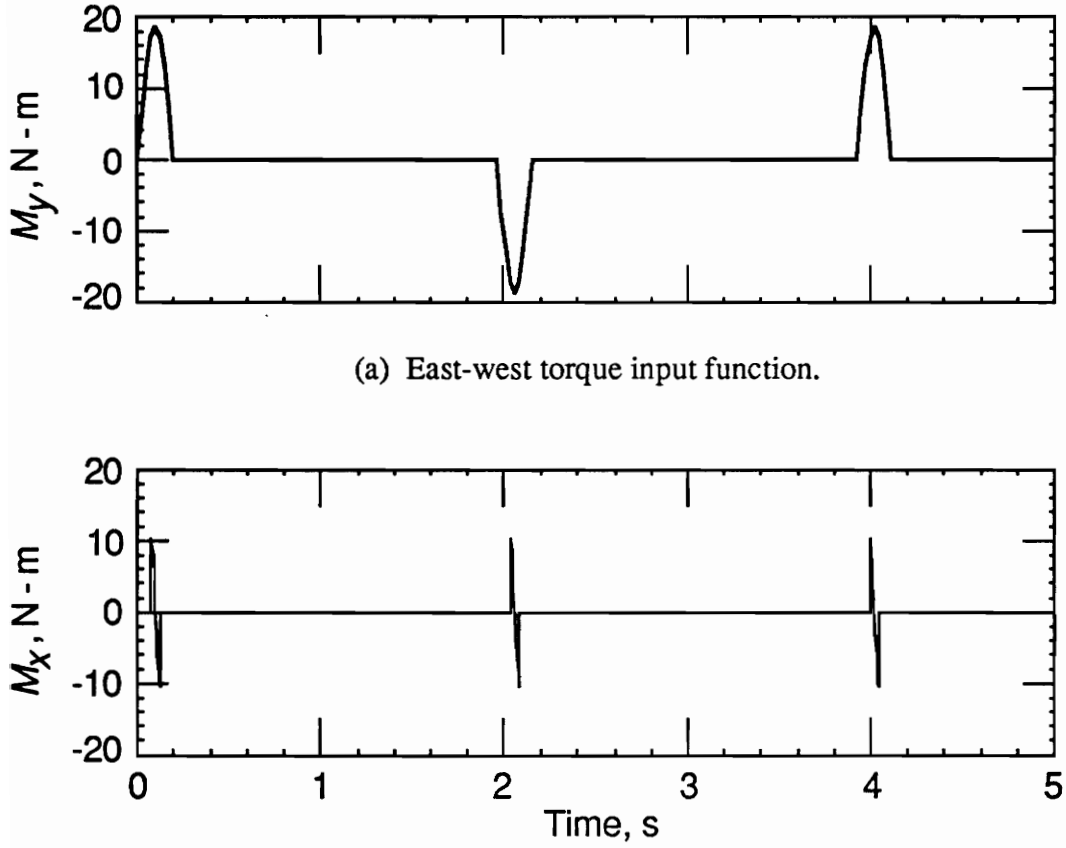

(a) East-west torque input function.

(b) North-south torque input function.

Figure 25. The first 5 seconds of scanning torque excitation functions.

The input torque disturbance function M_x is therefore

$$M_x = 5.137 \cos \left[\frac{\pi(t\text{-}0.0737)}{0.0491}\right] \text{ N-m} \qquad (2)$$

The north-south disturbance is always applied in the positive sense during the operational scan to facilitate the progression of the scan from the northernmost line to the southernmost line. The transient torque equation for the north-south motion is in effect during the time period 0.0737 s $\leq t \leq$ 0.1228 s (Figure 24, point C to point D), whereas the north-south displacement θ_x and therefore the input torque M_x are zero during the rest of the line scan: 0 s $\leq t \leq$ 0.0737 s (Figure 24, point B to point C) and 0.1228 s $\leq t \leq$ 1.965 s (point D to point F). The function is applied concurrently with the east-west function. The north-south function is plotted in Figure 25(b).

Reset Maneuver

A representative 15 lines of scan were found to be sufficient to quantify the dynamic behavior of the antenna. Along with the 15 lines of operational scan, a nonoperational reset maneuver is modeled and incorporated into the analysis. The purpose of this maneuver is to reset the subreflector from its position at the end of an Earth-disk scan (Figure 24, point G) to its proper position to begin the next Earth-disk scan (Figure 24, point A). Since no measurements are made during this maneuver, the reset also serves as an indicator to the data recorders of the end of one Earth-disk scan and the beginning of the next. This study assumes that the reset maneuver takes the same amount of time as one line of scan (t_l). This diagonal maneuver is broken down into its orthogonal components below.

East-west component. The east-west component of the reset maneuver is modeled simply as another line of scan. The moment input function to begin the reset is merely a negative cosine pulse identical in magnitude to that of Eq. (1), whereas the input to end the reset and begin the next Earth-disk scan is a positive pulse of Eq. (1).

North-south component. The modeling of the north-south component of the reset maneuver differs from that of the east-west component in several ways. The north-south angular velocity component immediately prior to the reset is $\omega_x = 0$ deg/s, unlike the east-west angular velocity component which is $\omega_y = -3.716$ deg/s. Therefore, the north-south reset pulse component does not need to first decelerate the subreflector to zero as does the east-west component. Also, the overall geometry of the antenna and the geostationary platform must be considered. Care must be taken to avoid excessive torque inputs about the x-axis, since this is the axis about which there is least inertia. (See Figure 1.) Consequently, extreme torques about this axis are likely to induce excessive rocking about the x-axis.

The north-south component is therefore assumed to be a single large "step" from the southernmost line back up to the northernmost line, modeled in a manner similar to the individual north-south steps of the operational scan. This manner of north-south reset results in a low-acceleration motion of the subreflector throughout the 1.965 s of the maneuver, unlike the east-west reset which is composed of a relatively large acceleration pulse followed by a long period of zero-acceleration coasting. The north-south reset component is formulated as follows:

$$\theta_{x,\text{reset}} = -7.3 \cos \left[\frac{\pi(t-0.0737)}{1.965}\right] \text{ deg}$$

$$\omega_{x,\text{reset}} = 11.671 \sin\left[\frac{\pi(t-0.737)}{1.965}\right] \text{ deg/s}$$

$$\dot{\omega}_{x,reset} = 18.659 \cos\left[\frac{\pi(t-0.737)}{1.965}\right] \text{ deg/s}^2$$

$$M_{x,\text{reset}} = -5.862 \cos\left[\frac{\pi(t-0.737)}{1.965}\right] \text{ N-m}$$

Note that $M_{x,\text{reset}}$ must be applied in the negative direction to bring the subreflector from the southernmost line back to the northernmost line. The north-south reset component pulse is less severe than that of the east-west component since the velocity changes slowly over the course of the entire reset maneuver, rather than changing quickly at the beginning of the line and then coasting for the rest of it. The input to begin the first line of the next Earth-disk scan is then simply a pulse equal to Eq. (2).

Chapter 5. Antenna Structural Analysis

A static analysis of the LFMR has been made by L. F. Rowell and G. D. Qualls of the Langley Research Center in presently unpublished data. The dynamic performance analysis of the LFMR in the present paper consists of using the flexible modes and corresponding natural frequencies of each configuration as determined by the modal analysis, along with the torque inputs from the subreflector scan, to perform a forced-response analysis. (Note that the rigid-body modes, described in Chapter 3, do not contribute to the elastic deformation of the antenna. The six rigid-body modes were therefore deactivated for the forced response analysis so that only the flexible modes for each configuration contributed to the response.) In line with the conservative nature of this study, internal structural damping was assumed small (0.5 percent). The resulting dynamic displacements are then used to quantify the antenna geometric errors. The LFMR performance is evaluated in terms of the effect that the surface node distortions have on the rms surface roughness, pointing error, and defocus, the effect that the subreflector displacement has on the pointing error and defocus, and the effect that the displacement of the reflector vertex has on the defocus.

Geometric Performance Criteria

The electromagnetic performance of an antenna can be adversely affected by numerous factors. Among these is the geometric displacement of the various structural components of the antenna from their optimum positions. Minimizing the overall surface roughness, pointing error, and defocus is of extreme importance for high-precision reflector antennas such as the LFMR.

Surface roughness. The surface roughness of a reflector antenna is defined as the root mean square (rms) of the reflector surface distortions relative to the best-fit paraboloid through the distorted surface locations. The maximum allowable rms surface roughness for an antenna can generally be related to both the wavelength λ of its highest operating frequency and to its application. For Earth-scanning radiometer systems such as the LFMR, the allowable rms error has been specified to be within the range from $\lambda/50$ to $\lambda/100$ ([35] and [36], respectively). The $\lambda/100$ limit was used for this analysis to provide the more conservative requirement. The 37-GHz LFMR operating frequency therefore has a maximum allowable rms error of 8.11×10^{-5} m (3.2 mils).

Pointing error. In the present study, the pointing error of a reflector antenna consists of two parts: the angular rocking of the primary reflector and the physical displacement of the feed mast. Angular rocking is defined as the rotation of the best-fit paraboloid relative to the original undistorted paraboloid and is referred to here as "the pointing error due to surface distortion." Feed mast displacement contributes to the pointing error because displacing the feed and/or subreflector laterally from their optimum positions with respect to the Cassegrain geometry repoints the emitted beam. For the present LFMR configuration, the subreflector and feed are sufficiently close for their relative displacements to be considered negligible. The subreflector contribution to the pointing error is therefore calculated as the change in the angle that the subreflector makes with the axis of symmetry of the undistorted paraboloid (i.e., the z-axis).

The combination of these pointing errors is illustrated in Figure 26, which shows that the combined pointing error about the x-axis Φ_x is as follows:

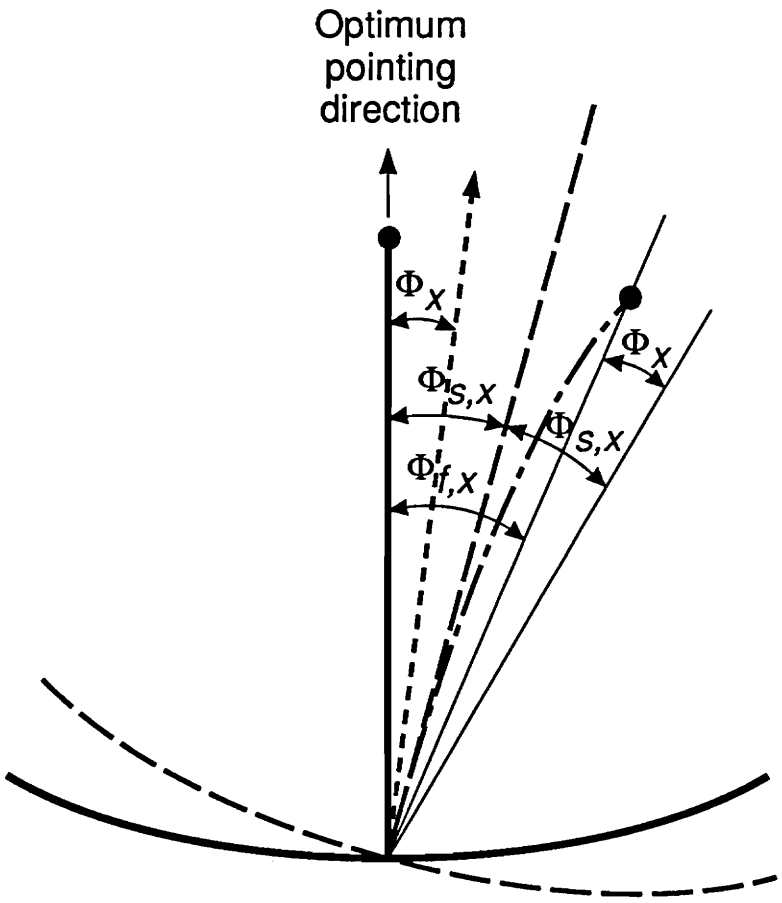

● Feed/subreflector system

Undistorted antenna

Best-fit paraboloid and its axis of symmetry

Distorted feed mast

Pointing direction of distorted antenna system

$\Phi_{s,X}$ = Pointing error about *x*-axis due to surface distortion

$\Phi_{f,X}$ = Pointing error about *x*-axis due to subreflector (i.e., feed mast) displacement

$\Phi_X = 2\Phi_{s,X} - \Phi_{f,X}$ = Combined pointing error about *x*-axis

Figure 26. Definition of pointing error.

$$\Phi_x = 2\Phi_{s,x} - \Phi_{f,x} \tag{3}$$

where $\Phi_{s,x}$ is the pointing error due to the surface distortion (i.e., angular rocking of the primary reflector) and $\Phi_{f,x}$ is the pointing error due to the subreflector (i.e., feed mast) displacement. Similarly, about the y-axis,

$$\Phi_y = 2\Phi_{s,y} - \Phi_{f,y} \tag{4}$$

The magnitude of the total LFMR pointing error Φ_t is equal to the angle between the pointing direction of the distorted antenna and the optimum pointing direction (the axis of symmetry of the undistorted paraboloid) and is found by

$$\Phi_t = \cos^{-1}(\cos \Phi_x \cos \Phi_y) \tag{5}$$

The maximum allowable pointing error for the LFMR was assumed to be 10 percent of the beamwidth [31], and, like the surface roughness, the pointing error is dependent on the highest operating frequency. The pointing error limit is 6.22×10^{-5} rad (12.83 arcsec).

An additional factor that may contribute to the total antenna pointing error is the redirection of the subreflector caused by localized bending of the feed mast. Since the mechanism by which the subreflector will be connected to the mast has not yet been determined, this issue is not addressed in detail in the present study, which assumes that a rigid connection exists between the subreflector and feed mast.

Defocus. The defocus of an antenna consists of three parts: the difference between the focal length of the best-fit paraboloid and that of the undistorted reflector, the translation of the feed and subreflector along the axis of symmetry, and the translation of the paraboloid vertex along the axis of symmetry. The total defocus in this first-order analysis is defined as the linear sum of these three factors. The maximum allowable defocus has been identified in the range from 0.2 to 2.0 times the wavelength of the highest operating frequency [31]. Using the more conservative requirement of 0.2λ yields a defocus limit of 1.62×10^{-3} m (63.9 mils).

Analysis Procedure

For each LFMR configuration, dynamic displacement data were calculated based on the input disturbance functions in the three translational DOF at a representative set of top-surface nodes (where the membrane is attached) as well as at the single subreflector node. The displacement data were then evaluated as to their effect on the optimum LFMR shape.

The subreflector displacement data were evaluated as previously described. The surface node displacement data were used in conjunction with the Utku-Schmele best-fit paraboloid technique [29] to quantify the antenna performance in terms of its rms surface roughness, pointing error, and defocus. The Utku-Schmele technique calculates the geometric properties of the undistorted paraboloid reflector surface, as well as those of a new paraboloid which most closely fits through the distorted surface node positions. The rms error is then calculated based on the displacement of the distorted nodes from the best-fit paraboloid. The pointing error and defocus are quantified by comparing the new best-fit paraboloid axis of symmetry, focus, and vertex with those of the original, undistorted

paraboloid. The pointing error is output as the angular rocking of the dish about the x- and y-axes. The defocus results are given as the difference between the focal lengths of the distorted and undistorted paraboloids as well as the translation of the vertex in the focal direction.

Chapter 6. Results

The dynamic error curves are shown in Figures 27-32 for the free-flyer antenna and in Figures 33-38 for the platform-mounted antenna. Several general comments about these curves are given below, followed by specific descriptions of the individual error curves that are summarized in Table 8. Identification of specific modal contributions to the various errors is performed by close visual inspection of their cyclic trends and supported by fast Fourier transform analysis [37] of the error curves. For the pointing error and defocus curves, primary modal contributions are readily identified; however, specific modal contributions to the rms curves cannot be distinguished. Instead, the primary frequency contributing to the rms response appears to be the line frequency of the scan input (f_l = 0.509 Hz), as evidenced by the sharp peaks in the rms curves that occur at 1.965-s intervals. These peaks are also evident in the x-axis pointing error curves. For clarity, the error curves show the first 25 s of response. The effect of the reset is not shown since it was found to have minimal impact on the errors, increasing the magnitude of the x-axis pointing errors only. After the reset is completed, each of the errors continues to oscillate, eventually damping out to zero. In no case does the reset maneuver induce errors that are outside the specified limits.

Free-Flyer Antenna

Surface roughness. The rms surface roughness for the free-flyer antenna is shown in Figure 27. The rms error reaches a local maximum value at the time of application of each input torque, i.e., at approximately t_l intervals, and then begins to damp

Table 8. Summary of results.

Performance parameter	Assumed limit	Free-flyer		Platform-mounted	
		Maximum	Contributing modes	Maximum	Contributing modes
rms surface roughness, m	8.11×10^{-5}	5.3×10^{-6}	(a)	4.7×10^{-6}	(a)
Pointing error, rad	6.22×10^{-5}	1.9×10^{-5}	2, 3, 5 (x-axis) 1 (y-axis)	4.5×10^{-6}	2, 7 (x-axis) 1, 3 (y-axis)
Defocus, m	1.62×10^{-3}	1.3×10^{-4}	1	7.0×10^{-5}	1, 8

[a]Not applicable.

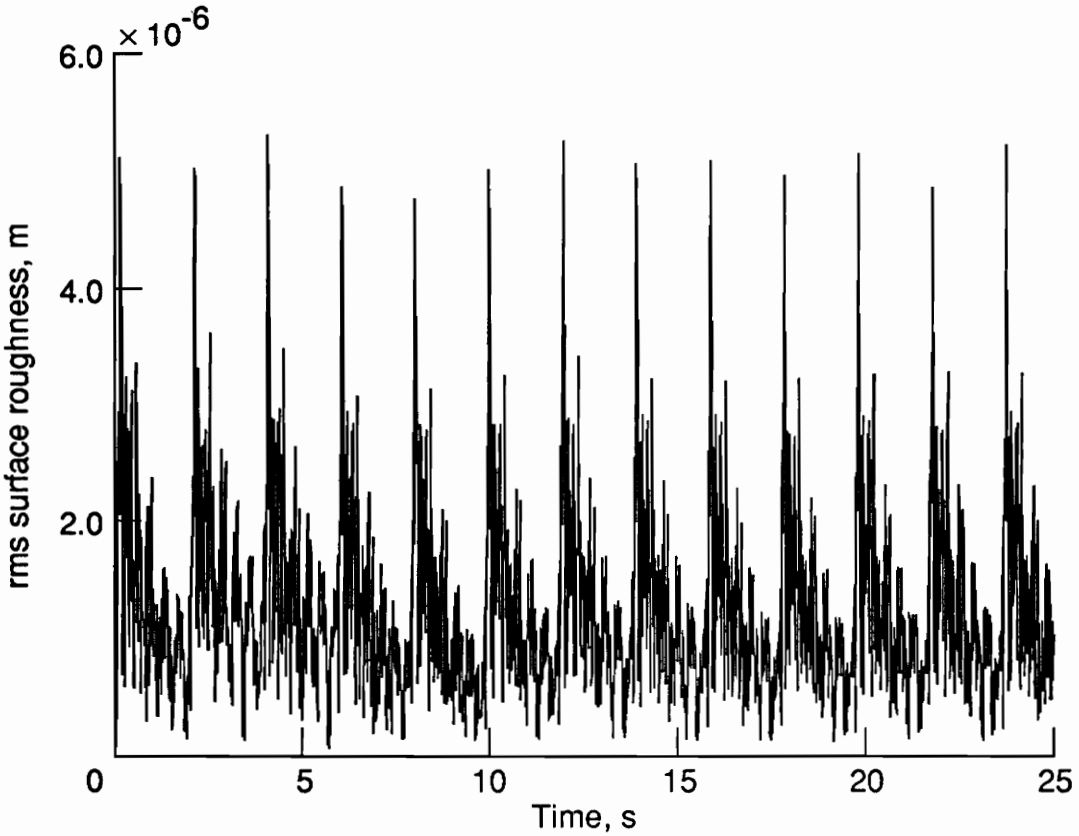

Figure 27. The rms surface roughness for the free-flyer antenna.

out until the subsequent torque is applied. The entire curve is well within the rms limit of 8.11×10^{-5} m, with its maximum magnitudes approximately 5.3×10^{-6}.

Pointing error. The pointing error about the x-axis is shown in Figures 28(a) and (b) for the surface and subreflector contributions, respectively, and in Figure 28(c) for the combined error about the x-axis, as determined by Eq. (3). These curves show insignificant errors during the scan input, with a maximum combined pointing error around 1.2×10^{-6} rad. As was seen in the rms curve, the maximum values in each of the three curves occur at the points of application of the input torques, and each maximum is followed by a damping motion until the next torque is applied. The combined curve exhibits behavior from modes 2, 3, and 5 (Figures 7, 8, and 10, respectively). Each of these contributing modes is an x-axis rocking-dominated mode. The pointing error about the y-axis is shown in Figures 29(a) for the surface contribution, 29(b) for the subreflector contribution, and 29(c) for the combined pointing error from Eq. (4). The combined-error curve has a maximum value of 1.9×10^{-5} rad and has the frequency of the first free-free mode (Figure 6), which is a rocking about the y-axis by both the surface and the subreflector.

The total LFMR pointing error for the free-flyer antenna as determined by Eq. (5) is shown in Figure 30. Note that this curve is a measure of the magnitude of the pointing error, not its direction. Torque application points are again seen as local maxima that damp out until the subsequent torque is applied. The maximum free-flyer pointing error is about 1.9×10^{-5} rad, which occurs primarily about the y-axis. This is well within the allowable limit of 6.2×10^{-5} rad.

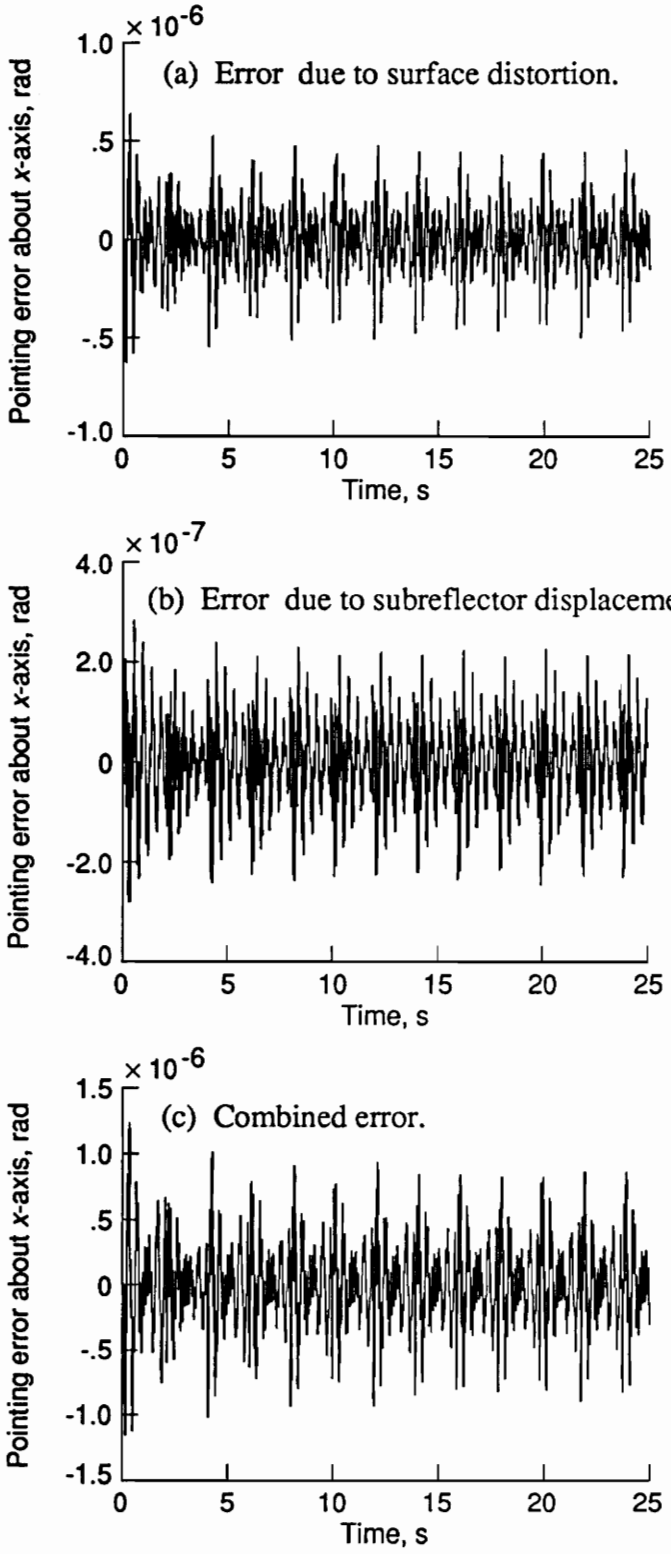

Figure 28. Pointing error about x-axis for free-flyer antenna.

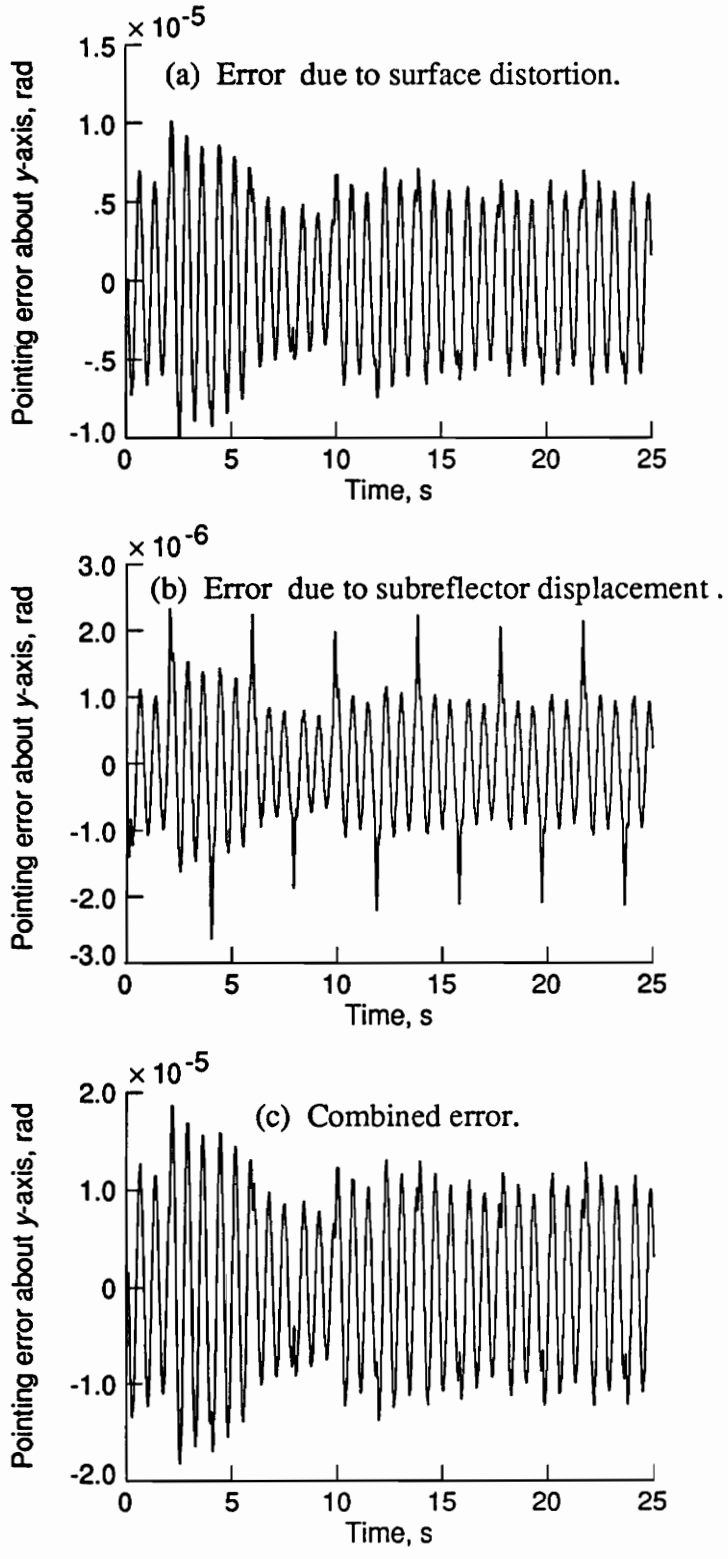

Figure 29. Pointing error about y-axis for free-flyer antenna.

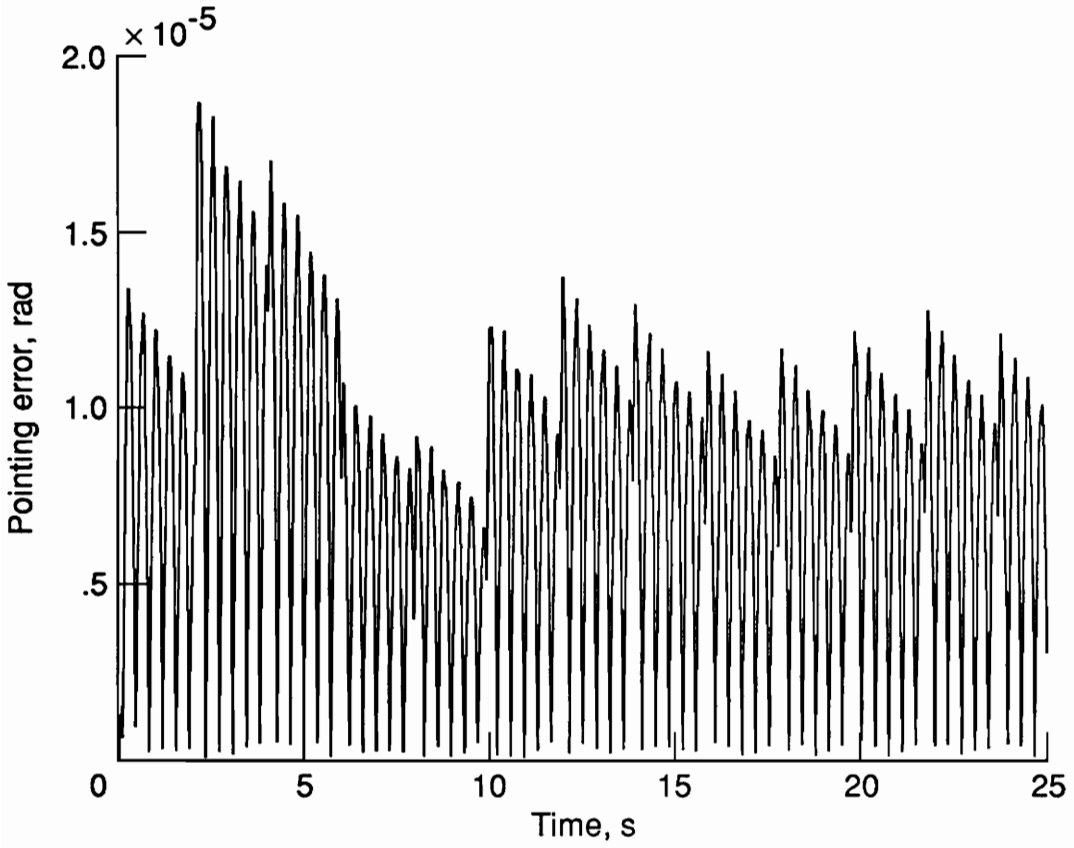

Figure 30. Total LFMR pointing error for the free-flyer antenna.

Defocus. The surface, subreflector, and vertex defocus curves are plotted in Figures 31(a), (b), and (c), respectively, with maximum defocus values of 5.8×10^{-5}, 4.7×10^{-5}, and 5.2×10^{-5} m, respectively. The sum of these curves is shown in Figure 32 and remains within the required limit of 1.62×10^{-3} m with a maximum defocus of 1.3×10^{-4} m. This curve shows a low-frequency response dominated by mode 1 (Figure 6), which includes a curling and flattening motion in the dish and a movement of the subreflector both toward and from the dish surface.

Platform-Mounted Antenna

Surface roughness. The rms surface roughness for the platform-mounted configuration is plotted in Figure 33 and is well within the specified rms limit with a maximum of about 4.7×10^{-6} m. As in the free-flyer case, the points of the input disturbances are the points of maximum rms error. These errors then damp out during the steady-motion portion of the subreflector scan and again spike to maximum values at the next turnaround.

Pointing error. The pointing error about the x-axis caused by the surface, subreflector, and combined displacements, respectively, are illustrated in Figures 34(a), (b), and (c). The combined curve in Figure 34(c) has a maximum value of 2.7×10^{-6} rad, and it exhibits mode 2 and mode 7 behavior (Figures 16 and 21, respectively). The curves exhibit a reaction at the point of application of the torque similar to that of the free-flyer case. The pointing error increases to a local maximum and then damps down until the next torque is applied. The subreflector curve in Figure 34(b), however, exhibits an additional response: the application of the torque appears to excite higher frequency modes that damp

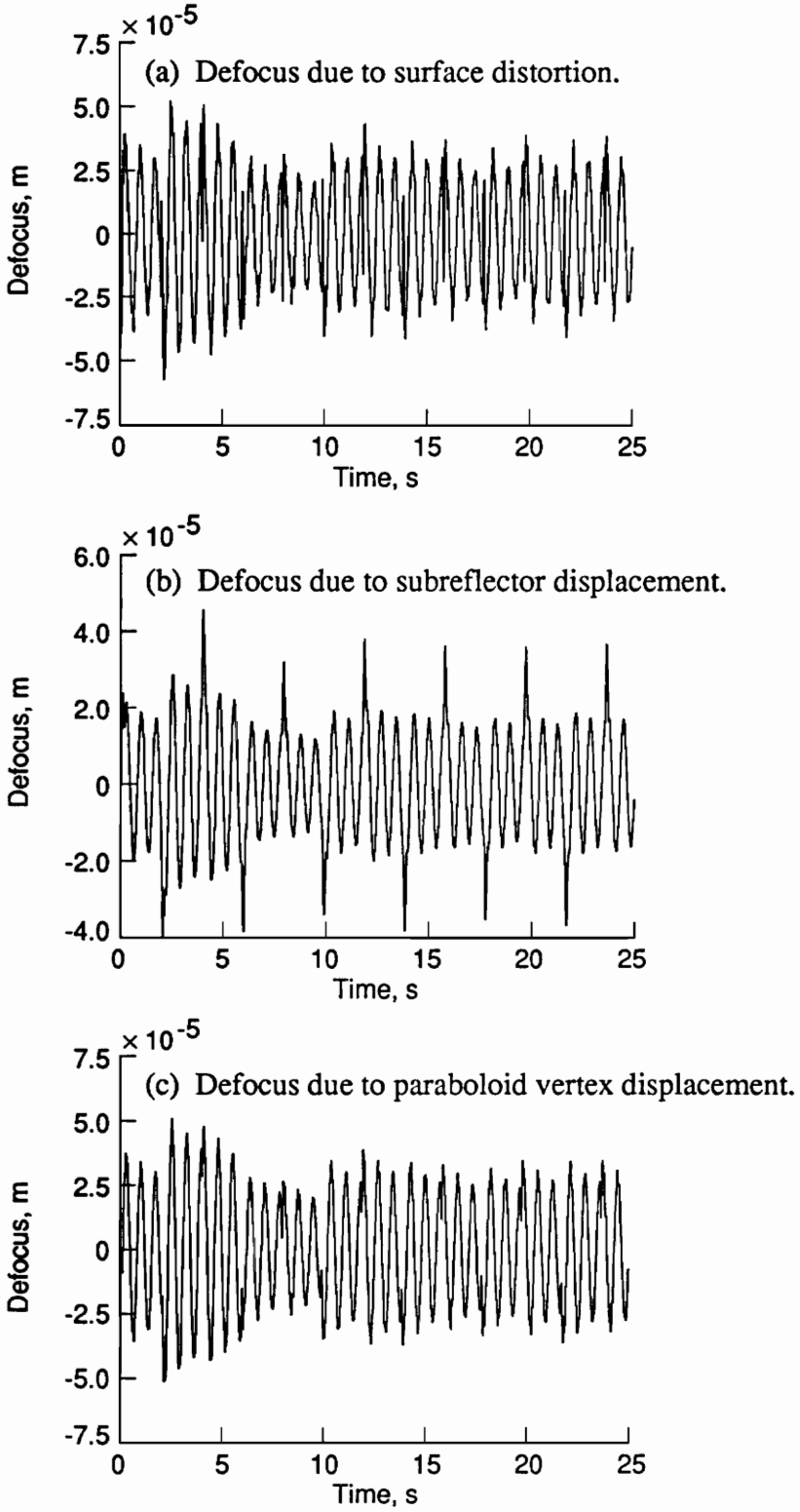

Figure 31. Defocus for free-flyer antenna.

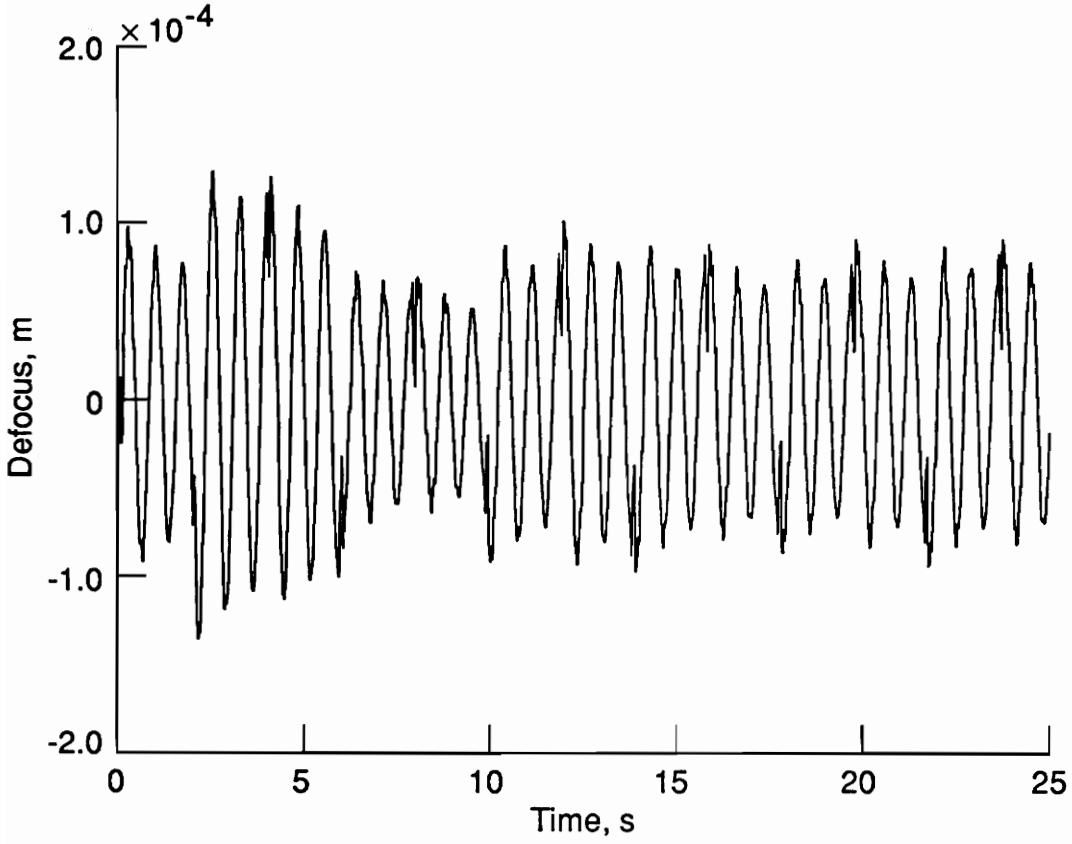

Figure 32. Total LFMR defocus for the free-flyer antenna.

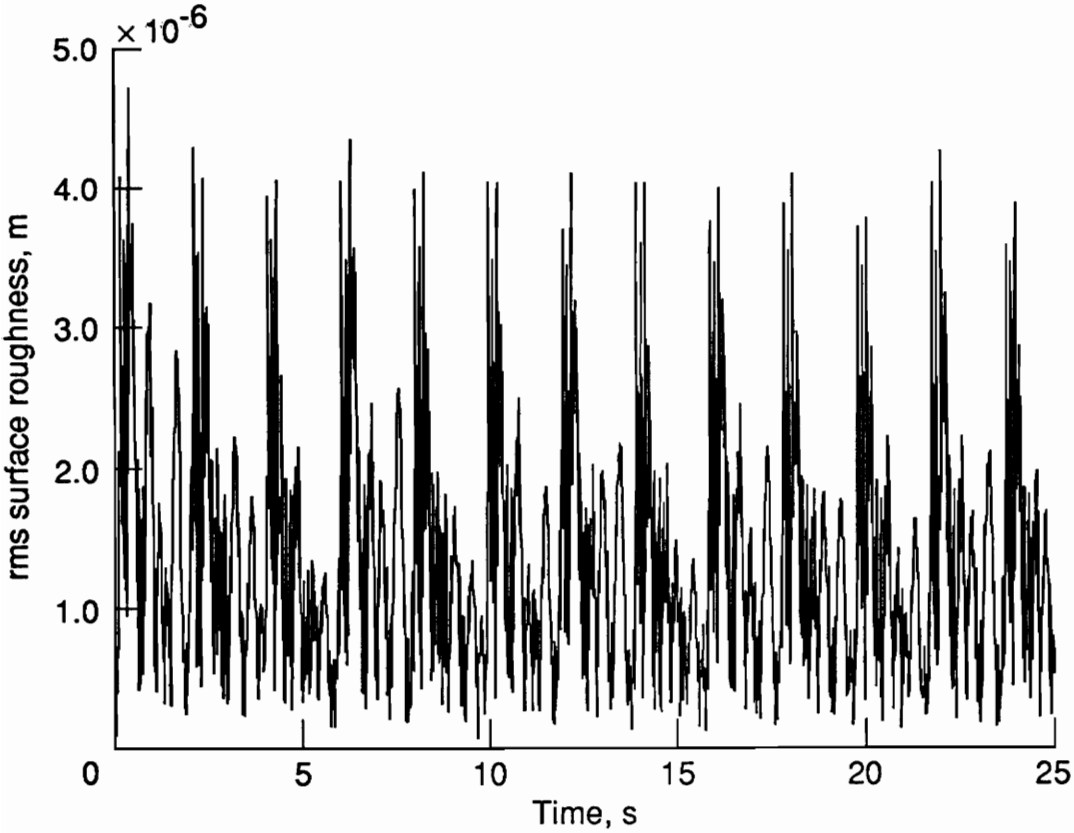

Figure 33. The rms surface roughness for the platform-mounted antenna.

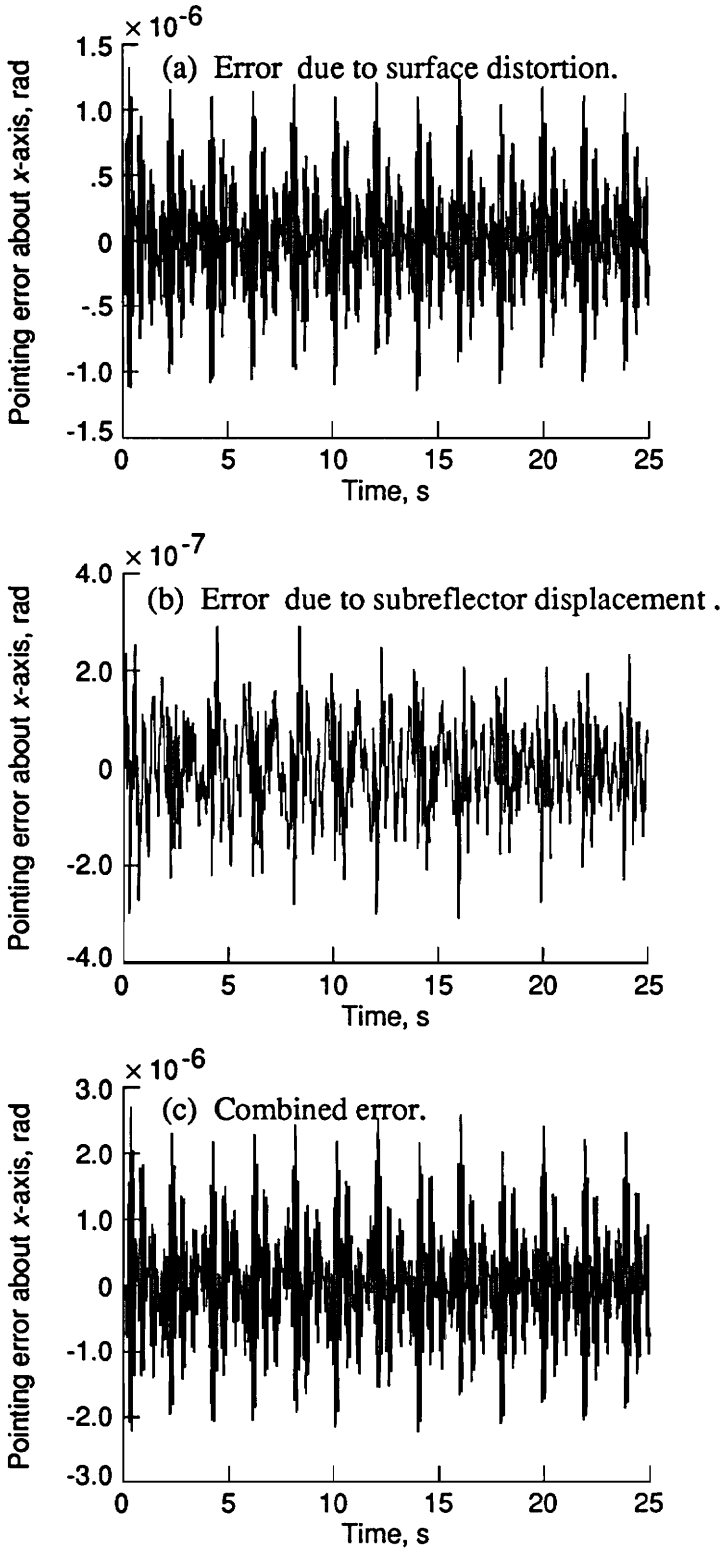

Figure 34. Pointing error about x-axis for platform-mounted antenna.

out quickly before the subsequent excitation occurs. The pointing error about the *y*-axis is shown in Figures 35(a), (b), and (c) for the surface, subreflector, and combined distortions, respectively. The combined response is shaped by modes 1 and 3 (Figures 15 and 17) for the surface curve and has a maximum value of 4.5×10^{-6} rad.

The total pointing error from Eq. (5) for the platform-mounted LFMR is shown in Figure 36. Again, there are local maxima at the torque application points that damp out until the subsequent torque input. The maximum platform-mounted pointing error is approximately 4.5×10^{-6} rad, which is about one-fourth that of the free-flyer configuration because of the cantileverlike connection to the platform, which has a large inertia about the *y*-axis relative to the *x*-axis. This connection inhibits rotation about the *y*-axis which, for both the free-flyer and platform-mounted configurations, is the primary contribution to the total pointing error. Therefore, the total pointing error is lower for the platform-mounted configuration than for the free-flyer configuration.

Defocus. The defocus curves are plotted in Figures 37(a), (b), and (c), respectively, for the surface, subreflector, and vertex defocus errors with maximum magnitudes of 7.0×10^{-5}, 2.4×10^{-5}, and 2.6×10^{-5} m, respectively. The total defocus is plotted in Figure 38 with a maximum total error of 7.0×10^{-5} m. This curve has both high- and low-frequency characteristics exhibiting mode 1 and mode 8 behavior (Figures 15 and 22, respectively) and remains well within the defocus limit of 1.62×10^{-3} m. The platform-mounted defocus is much smaller than the free-flyer defocus, again because of the cantileverlike connection to the platform mass that causes the reflector to remain relatively fixed and bend about the platform connection region.

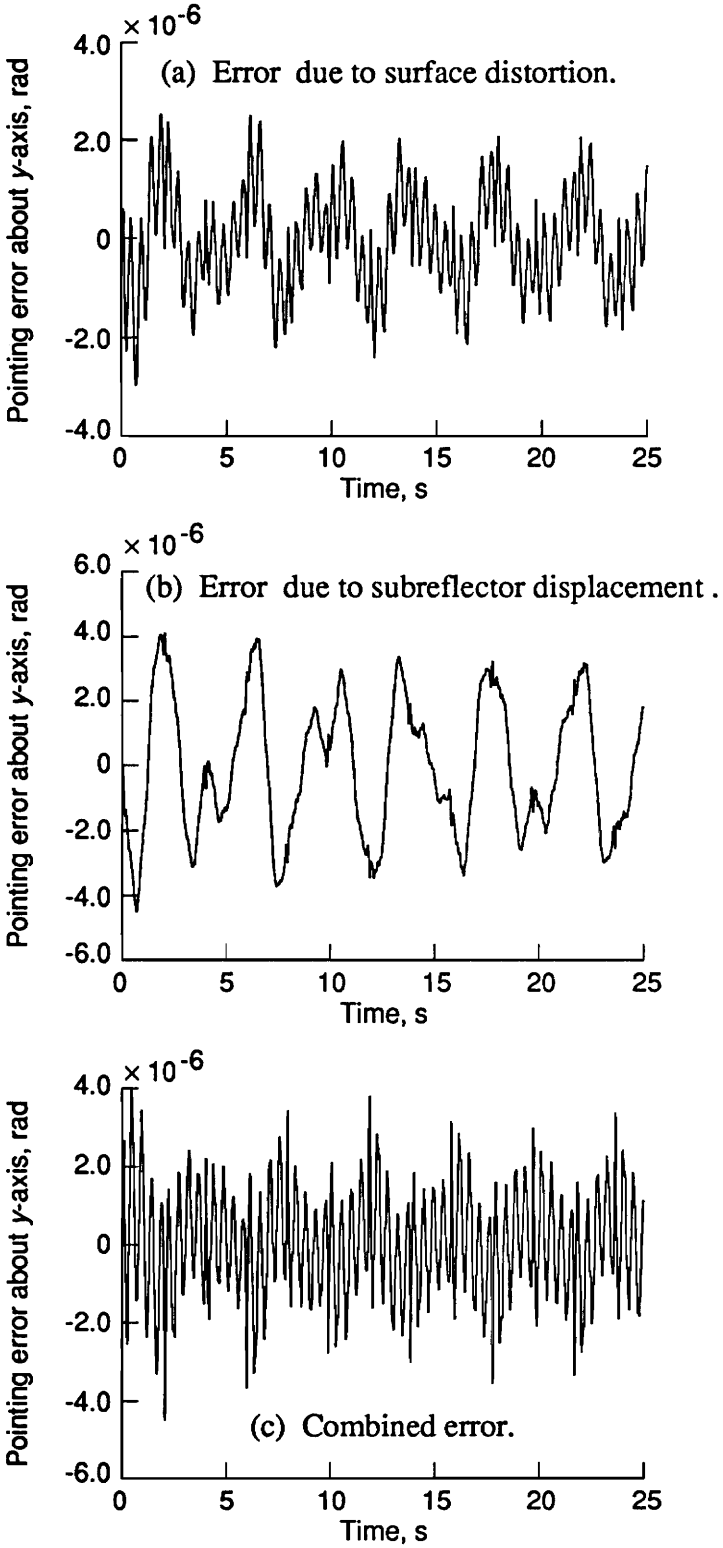

Figure 35. Pointing error about *y*-axis for platform-mounted antenna.

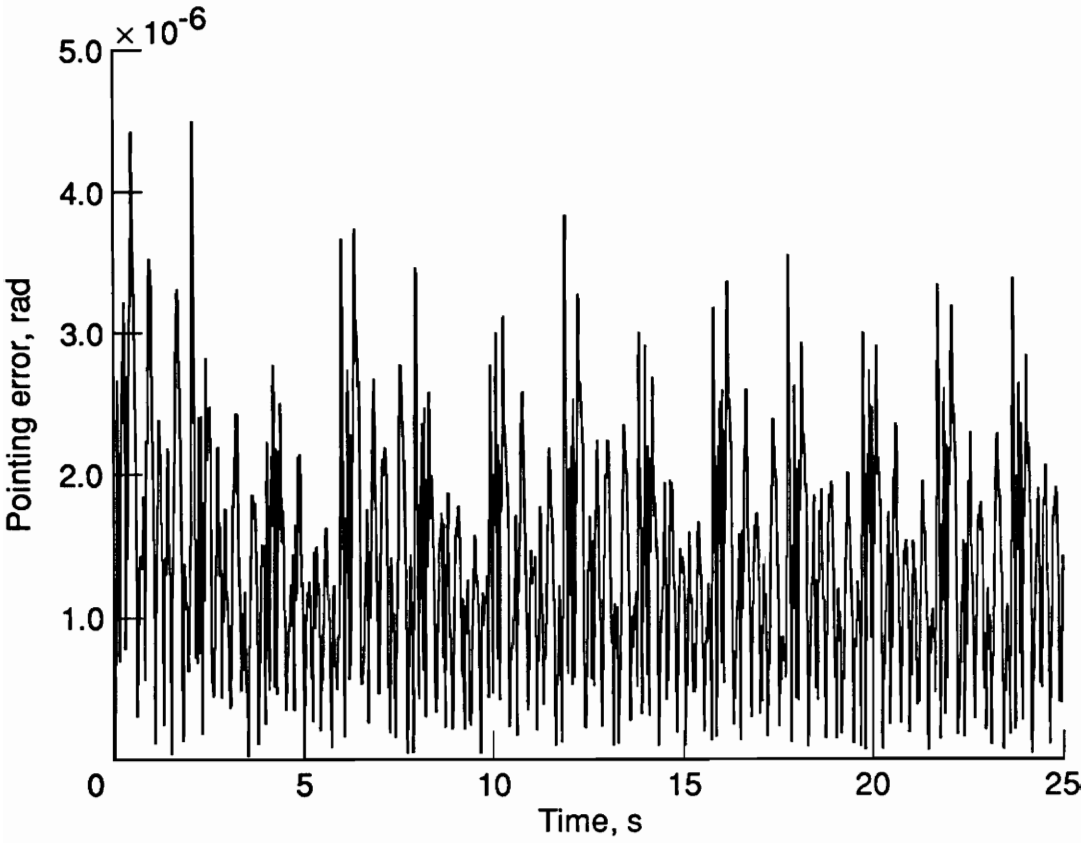

Figure 36. Total LFMR pointing error for the platform-mounted antenna.

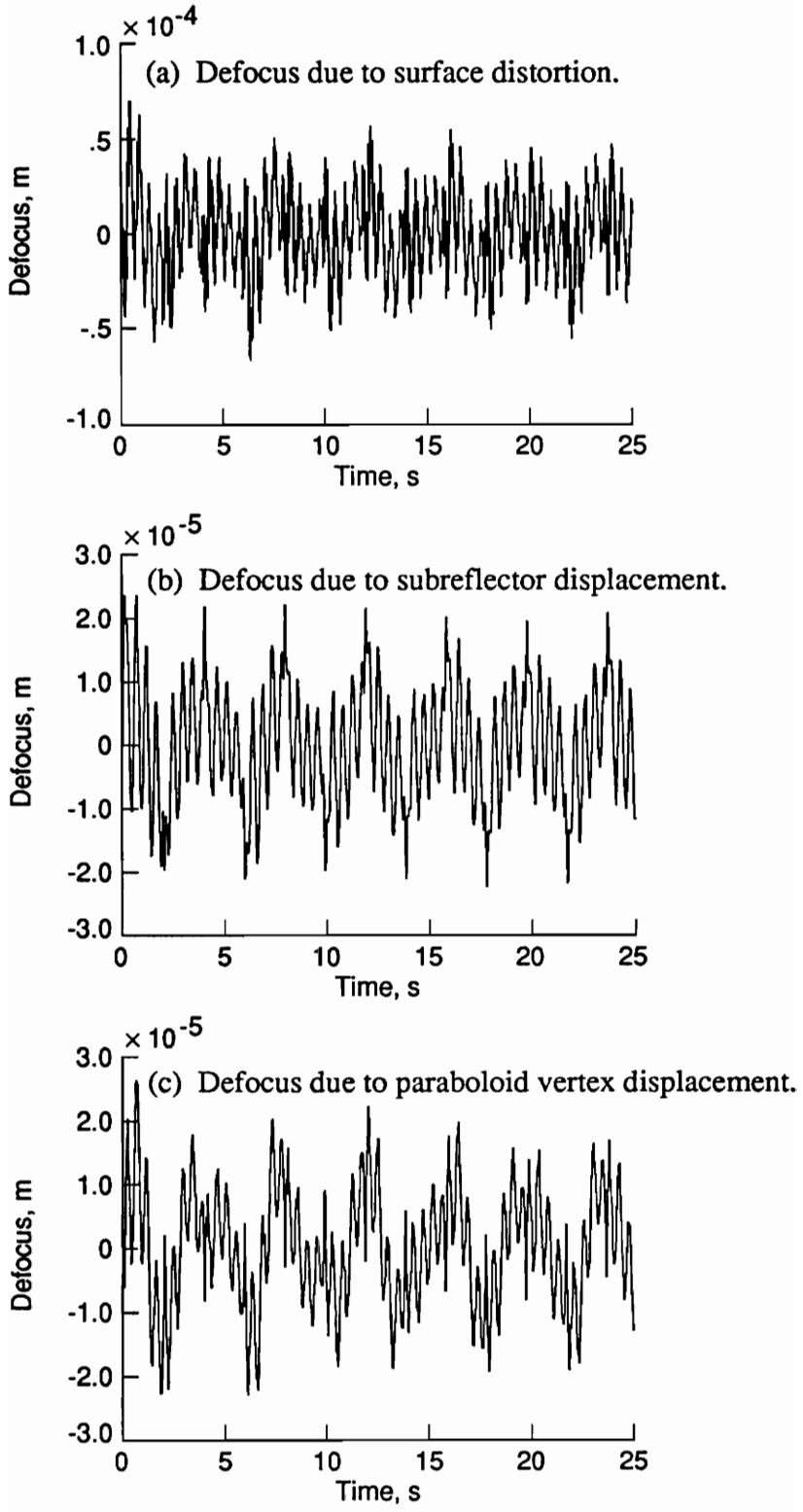

Figure 37. Defocus for platform-mounted antenna.

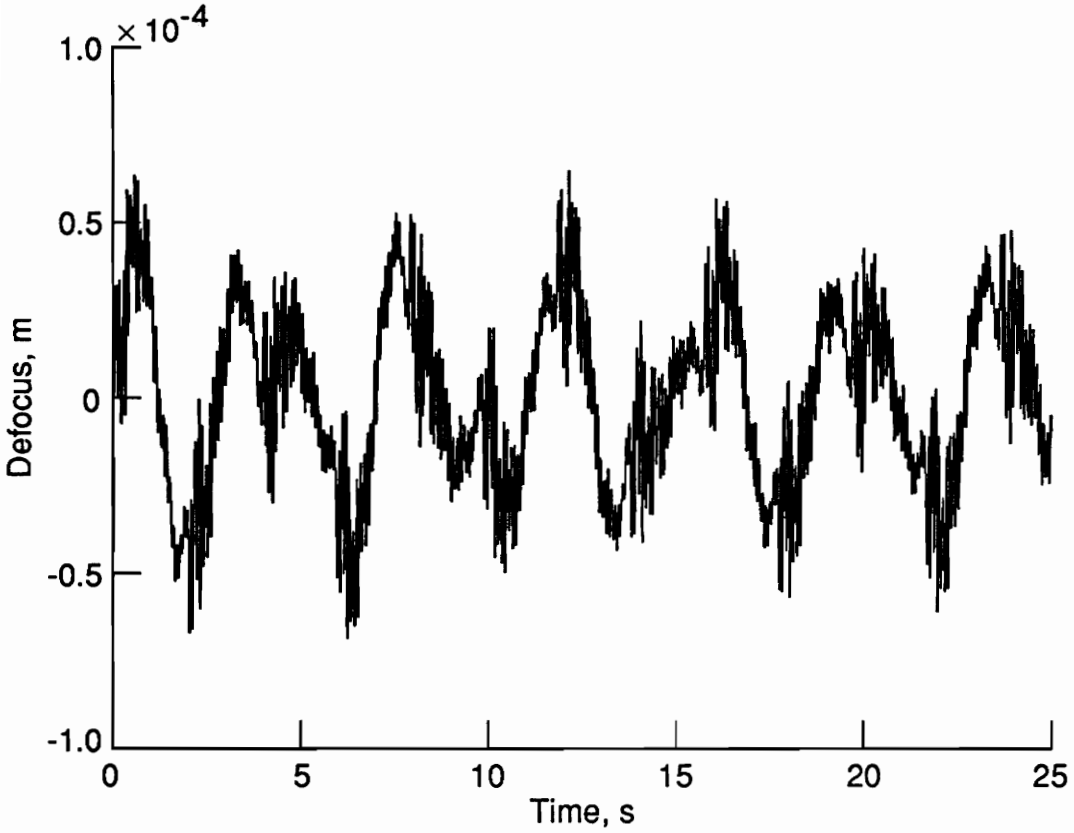

Figure 38. Total LFMR defocus for the platform-mounted antenna.

Chapter 7. Concluding Remarks

Analyses were conducted to determine the performance of a low-frequency microwave radiometer located on a geostationary platform subject to representative onboard disturbances. Parameter limits on antenna performance were defined for the root-mean-square surface roughness, pointing error, and defocus. The antenna concept and science requirements were defined and a finite-element model was generated. A subreflector scanning scenario was developed, consisting of a 30-min Earth-disk scan with a 10-km footprint, and corresponding input excitation functions were modeled representing the onboard disturbances to the system. A modal analysis was performed on the antenna for two configurations: free-flying and platform-mounted. The resulting mode shapes and natural frequencies were input to the forced-response analysis, which was performed for each configuration with the defined scanning disturbance. The forced-response analysis then quantified the dynamic distortions and their impact on the performance parameters was assessed. The distortions in the surface contributed to all three errors, the displacement of the subreflector added to the pointing error and defocus, and the displacement of the vertex was a component of the defocus.

The results of this analysis indicate that the strongback and feed mast of the low-frequency microwave radiometer (LFMR) as designed are capable of maintaining their shapes within specifications for the assumed on-orbit disturbance, particularly in the platform-mounted configuration which exhibited errors within their respective limits by at least an order of magnitude. This was also true for the free-flyer surface roughness and defocus; however, the free-flyer maximum pointing error was significantly closer to, yet still within, its specified limit.

These results indicate that active or passive control techniques may not be necessary for the present LFMR design. It must be noted, however, that these results are based on the assumption of an "ideal" reflector, i.e., that there is no slop in the joints from either manufacturing errors or deployment and that there is no "pillowing" of the membrane reflector surface. Additionally, localized feed mast bending is not addressed here and may adversely affect overall antenna pointing. Various attachment mechanisms must be examined so as to minimize this effect. The present study also does not include the effects of the geostationary thermal environment, which, in addition to the dynamic disturbance examined here, may cause the errors to exceed the specified limits. Other sources of vibration, such as the spacecraft attitude control subsystem, must be considered and examined. Care must be exercised in devising scan scenarios and momentum compensation so as to minimize both the torques that are input to the system due to subreflector rotation and the concurrence of torque input frequencies with the natural frequencies of the system. This includes careful selection of retrace time, footprint size, the details of each line of scan (i.e., the time allotted for turnaround and step-down procedures), and component masses.

Recommendations for future studies therefore include: (1) determining manufacturing error tolerances; (2) identifying the extent of "pillowing" of the reflector surface and determining the impact on antenna performance; (3) investigating various means of attaching the feed and subreflector to the feed mast and quantifying the effects of localized feed mast bending on pointing error; (4) assessing the thermal effects of geostationary orbit on the structural behavior of the antenna; (5) identifying other vibration-inducing sources and quantifying the resulting distortions; and (6) devising a scanning technique that minimizes both the torques that are input to the system and the concurrence

of the torque input frequencies with the natural vibrational frequencies of the system while satisfying the mission science requirements.

References

1. Ride, Sally K., *Leadership and America's Future in Space--A Report to the Administrator of NASA*, Aug. 1987.

2. Pidgeon, David Joseph, *A Subsystem Design Study of an Earth Sciences Geostationary Platform*, M.S.Thesis, George Washington Univ., July 1989.

3. Ford Aerospace Corp., *Geostationary Platform Bus Study for Earth Observation Sciences. Volume II--Comprehensive Report, Final Report*, Sections 1.0 thru 10.0, WDL--TR 11066 (Contract NAS8-36104), Sept. 1987.

4. Farmer, Jeffery T., Wahls, Deborah M., and Wright, Robert L., *Thermal-Distortion Analysis of an Antenna Strongback for Geostationary High Frequency Microwave Applications,* NASA TP-3016, 1990.

5. Meirovitch, Leonard, *Elements of Vibration Analysis*, McGraw-Hill Book Company, 1986.

6. Bathe, K. J., *Finite Element Procedures in Engineering Analysis*, Prentice-Hall, Inc., 1982.

7. Cook, R. D., *Concepts and Applications of Finite Element Analysis*, John Wiley and Sons, Inc., 1974.

8. Gallagher, R. H., *Finite Element Analysis Fundamentals*, Prentice-Hall, Inc., 1975.

9. Zienkiewicz, O. C., *The Finite Element Method*, Third edition, McGraw-Hill Book Company, 1977.

10. Martin, H. C., *Introduction to Matrix Methods of Structural Analysis*, McGraw-Hill Book Company, 1966.

11. Przemieniecki, J. S., *Theory of Matrix Structural Analysis,* McGraw-Hill Book Company, 1968.

12. Rubenstein, M. F., *Matrix Computer Analysis of Structures*, Prentice-Hall, Inc., 1966.

13. Vanderbilt, M. D., *Matrix Structural Analysis*, Quantum Publishers, Inc., 1974.

14. *MSC/NASTRAN User's Manual*, Version 66A, The MacNeal-Schwendler Corporation, Nov., 1989.

15. *PATRAN Plus User's Manual*, Release 2.3, Publication No. 2191020, PDA Engineering, July, 1988.

16. Whetstone, W. D., *EISI-EAL Engineering Analysis Language Reference Manual*, Engineering Information Systems, Inc., July, 1983.

17. DeRyder, Leonard J., Space Station Integrated Computer-Aided Engineering Systems Analysis Software, *NCGA's Computer Graphics '87, Eighth Annual Conference and Exposition--Proceedings, Volume III--Technical Sessions,* National Computer Graphics Assoc., 1987, pp. 249--262.

18. Lu, Chu-Ho, *Study of the Available Finite Element Software Packages at KSC*, NASA CR-187638, Sept., 1990.

19. Fortin, P. E., *Economic Evaluation of Computerized Structural Analysis*, NASA CR-177078, Aug., 1985.

20. Hall, R. L., and Radhakrishnan, N., *CASE (Computer-Aided Structural Engineering) Study of 6 Major General-Purpose Finite Element Programs, Final Technical Report*, Report #AD-A139065, Oct., 1983.

21. Anderson, G. C., Garrett, L. B., and Calleson, R. E., *Comparative Analysis of On-Orbit Dynamic Performance of Several Large Antenna Concepts*, AIAA-85-0818-CP, April, 1985.

22. Garrett, L. B., and Ferebee M. J., *Comparative Analysis of Large Antenna Spacecraft Using the IDEAS System*, AIAA-83-0798-CP, 1983.

23. D'Cruz, P. B., *Space Station Dynamic Analysis*, Society for Experimental Mechanics, Inc., 5th International Modal Analysis Conference Proceedings, London, England, April 6-9, 1987.

24. Garrison, J. L., and Rowell, L. F., *Launch Vehicle Integration Options for a Large Earth Sciences Geostationary Platform Concept*, NASA TP-3083, 1991.

25. Leondis, Alex, *Large Advanced Space Systems Computer-Aided Design and Analysis Program--Final Technical Report*, NASA CR-159191-1, 1980.

26. *Supertab--Engineering Analysis Pre- and Post-Processing User Guide,* I-DEAS Level 4, Structural Dynamics Research Corp., 1988.

27. *Supertab--Engineering Analysis Model Solution and Optimization User Guide,* I-DEAS Level 4, Structural Dynamics Research Corp., 1988.

28. *Systan--Engineering Analysis System Dynamics User Guide*, I-DEAS Level 4, Structural Dynamics Research Corp., 1988.

29. Ludwig, A., ed., *Computer Programs for Antenna Feed System Design and Analysis--Volume I: Programs and Sample Cases,* NASA CR-84810, 1967.

30. Lockheed Missiles & Space Co., Inc., *Geostationary Platform Study--Contract Extension, Final Report,* LMSC-F278679, Rev. A (Contract NAS8-36103, Modification No. 13, DR-9), Nov. 1988.

31. Dyer, J. E., *Development of a Verification Program for Deployable Truss Advanced Technology*, NASA CR-181703, 1988.

32. Adams, Louis R., *Design, Development and Fabrication of a Deployable/Retractable Truss Beam Model for Large Space Structures Application*, NASA CR-178287, 1987.

33. Collins, Timothy J., and Fichter, W. B., *Support Trusses for Large Precision Segmented Reflectors--Preliminary Design and Analysis*, NASA TM-101560, 1989.

34. Foldes, Peter, *A Design Study for the Use of a Multiple Aperture Deployable Antenna for Soil Moisture Remote Sensing Satellite Applications,* NASA CR-178154, 1986.

35. Agrawal, Brij N., *Design of Geosynchronous Spacecraft*, Prentice-Hall, Inc., 1986.

36. Hedgepeth, John M., *Structures for Remotely Deployable Precision Antennas--Final Report*, NASA CR-182065, 1989.

37. Clough, Ray W., and Penzien, Joseph, *Dynamics of Structures*, McGraw-Hill, Inc., 1975.

Additional References Not Cited in the Text

Wahls, Deborah M., Farmer, Jeffery T., and Sleight, David W., *On-Orbit Structural Dynamic Performance of a 15-Meter Microwave Antenna*, NASA TP-3041, Dec., 1990.

Wahls, Deborah M., and Farmer, Jeffery T., *On-Orbit Structural Dynamic Performance of a Low-Frequency Microwave Radiometer for Mission to Planet Earth Applications*, AIAA-91-0428, Jan., 1991.

Vita

Deborah Marilyn Wahls is the daughter of Dr. and Mrs. Joseph Badi, born on December 2, 1964 in New York City. She received her Bachelor of Science degree in 1987 from Polytechnic University in Brooklyn, New York. Ms. Wahls has been employed at the NASA Langley Research Center in Hampton, Virginia since 1983 and is currently working in the Vehicle Analysis Branch of the Space Systems Division. She married Dr. Richard Alan Wahls on September 17, 1989.

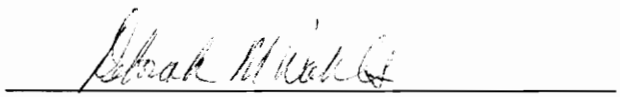

Deborah M. Wahls